

# Numerical investigation of the kinetics and chemistry of rf glow discharge plasmas sustained in He, N<sub>2</sub>, O<sub>2</sub>, He/N<sub>2</sub>/O<sub>2</sub>, He/CF<sub>4</sub>/O<sub>2</sub>, and SiH<sub>4</sub>/NH<sub>3</sub> using a Monte Carlo-fluid hybrid model

Timothy J. Sommerer<sup>a)</sup> and Mark J. Kushner<sup>b)</sup>

*Department of Electrical and Computer Engineering, University of Illinois, 1406 West Green Street, Urbana, Illinois 61801*

(Received 15 October 1991; accepted for publication 4 November 1991)

Capacitively coupled radio-frequency (rf) glow discharges are standard sources in plasma assisted materials processing. Theoretical analyses of rf discharges have been hampered by the computational difficulty of simultaneously resolving nonequilibrium electron transport and plasma chemistry. We have developed a hybrid Monte Carlo-fluid simulation that can simulate nonequilibrium electron transport while executing with the speed of a fluid simulation. An electron Monte Carlo simulation (EMCS) is used to calculate the electron energy distribution (EED) as a function of position and phase in the rf cycle. Collision rates and transport coefficients are calculated from the EED and used in a self-consistent fluid model (SCFM) of charged particle behavior and a neutral chemistry/transport model. Electric fields from the SCFM are cycled back to the EMCS, and the process is iterated until convergence. All pertinent heavy particle (charged and neutral) reactions can be included as well as collisions of electrons with ions, excited states, and reaction products. The hybrid model is applied to a variety of gas mixtures of interest to materials processing.

## I. INTRODUCTION

Radio-frequency (rf) glow discharges are routinely used for the etching and deposition of semiconductor materials during the fabrication of microelectronic devices.<sup>1</sup> Considerable effort has been expended to experimentally and theoretically characterize these discharges with the goal of obtaining a predictive capability for their operation.<sup>2-6</sup> The fundamental processes in rf discharges are fairly well understood. The manner in which these processes impact issues concerning control and optimization of discharge plasmas must still be resolved. The typical conditions of interest are gas pressures of tens of mTorr to a few Torr, power deposition of a few to hundreds of mW cm<sup>-3</sup>, and rf frequencies of hundreds of kHz to tens of MHz. These conditions result in bulk electron densities of 10<sup>9</sup>-10<sup>11</sup> cm<sup>-3</sup> and average electron energies of tenths to a few eV. A current challenge in designing plasma processing tools is the development of computer models of rf discharges that can accurately describe nonequilibrium charged particle transport and plasma chemistry, yet execute quickly enough to make more realistic multidimensional simulations feasible. The goal is then to make discharge modeling an integral part of the discharge reactor design process.

Numerical modeling of rf discharges commonly uses one of two basic approaches: fluid or kinetic.<sup>2</sup> Fluid models solve Poisson's equation and one or more moments of Boltzmann's equation to obtain (for a three-moment fluid model) the density, momentum, and energy of each

charged species.<sup>7-9</sup> These models tend to be robust, meaning that they execute fairly rapidly and can address a wide range of discharge conditions. The assumptions inherent to the fluid approximations, though, generally restrict their application to plasmas where the mean free path for electron or ion collisions is small compared to the electrode separation. Recent studies have shown, however, that fluid models may be applicable at pressures below this limit provided that the total rate of ionization is well represented.<sup>10</sup> Fluid models do not typically resolve the electron energy distribution (EED), and assumptions must be made to relate the electron impact rate coefficients and transport coefficients to known fluid quantities such as E/N (the ratio of the electric field and the neutral gas number density) or  $\langle \epsilon \rangle$  (the mean electron energy).

Kinetic models such as particle-in-cell (PIC) simulations<sup>11,12</sup> and "convective schemes"<sup>13</sup> fully resolve the EED and the ion energy distribution (IED) as a function of space and time. These results are obtained by integrating Boltzmann's equation, either statistically (PIC) using Monte Carlo techniques for collisions, or directly as in the convective scheme. Nonequilibrium aspects of the EED and IED are well represented, and collective effects can be resolved. The disadvantage of kinetic models is that they are computationally intensive.

Hybrid models have been introduced as a method to speed computations while retaining important nonequilibrium aspects of the EED. Belenguer and Boeuf<sup>9</sup> first introduced this method for rf discharges in what is now termed a "beam-bulk" simulation. In this method, conventional fluid equations describe the ions and the low-energy "bulk" electrons. A second group of ballistic or "beam" electrons is used to represent secondary electrons that are emitted

<sup>a)</sup>Present address: General Electric, Research and Development, P.O. Box 8, Schenectady, NY 12301.

<sup>b)</sup>Author to whom correspondence should be addressed.

from the electrodes by ion, photon, and excited neutral impact, and are accelerated by the large sheath fields. The beam-bulk model can reproduce several essential features of high-voltage rf discharges, including the “ $\alpha$ -to- $\gamma$ ” transition.<sup>14,15</sup> Sato and Tagashira<sup>16</sup> have developed a hybrid model based on a combination of a Monte Carlo simulation and a fluid model. A Monte Carlo simulation is used to calculate excitation rate coefficients. These rate coefficients are incorporated into the fluid model by performing weighted integrals over the rf cycle which account for the finite response time of the EED to changes in the electric field. The rates obtained from the Monte Carlo portion of this model are not completely consistent with the fields and charge density used in the fluid model.

Truly hybrid models of dc discharges have been developed by Surendra, Graves, and Jellum<sup>17</sup> and Shoenbach, Chen, and Schaefer.<sup>18</sup> In these models, a Monte Carlo simulation (MCS) is used to generate electron impact rate coefficients which are then used in a fluid simulation. In the fluid simulation, the charge densities and electric fields are generated, which are then cycled back to the MCS. The process is repeated until convergence. The transport of excited states is typically not considered.

Porteous and Graves<sup>19</sup> have developed a hybrid model using a fluid model for electrons, and a particle representation for ions in a magnetically confined plasma such as that found in an electron cyclotron resonance (ECR) reactor. Electrons are magnetized in ECR reactors and have low mobilities transverse to the magnetic field lines compared to ions, whereas the ion mean free paths are commensurate with the size of the vessel. These conditions, and the fact that the fractional electron density is roughly 50–100 times that in conventional rf diode reactors, allows one to computationally separate the electrons and ions in the cited fashion. A similar technique was used by Weng and Kushner to calculate the EED in ECR reactors.<sup>20</sup> In their treatment, the electrons were treated as particles and the ions as a fluid.

Many nonequilibrium aspects of the EED in rf discharges have been demonstrated both experimentally and theoretically. It has been shown that the oscillation of the sheaths and secondary electron emission generate high-energy ballistic components to the EED which, in some cases, may dominate the excitation and ionization of the gas.<sup>13,21–23</sup> The periodic input of energy into this component of the EED causes the sites of excitation and ionization to oscillate across the discharge during the rf cycle. Such high-energy electrons can be responsible for the majority of the excitation and ionization in the discharge, but their density is sufficiently low that they do not significantly contribute to the overall charge balance. The vast majority of electrons have a relatively low mean energy and high collision frequencies,<sup>13,23,24</sup> and are therefore in quasiequilibrium with the electric field. It is these latter electrons that determine the conduction current and the charge densities. In fact, the total charge density needed to solve Poisson’s equation can be adequately represented by a fluid description for gas pressures  $\geq 100$  mTorr and rf frequencies less than a few tens of MHz.<sup>25</sup> Recognition of

this division of the EED into nonequilibrium and equilibrium components formed the basis of the beam-bulk model of Belenguer and Boeuf.<sup>9</sup>

To obtain a more generally applicable model for rf discharges it is desirable to accurately represent all of the nonequilibrium aspects of the EED. This representation can only be achieved by using a fully kinetic description for electron transport. A hybrid model that fully resolves the nonequilibrium aspects of the EED while using a fluid model to obtain charge densities can be reliably used at significantly lower pressures and higher rf frequencies than a pure fluid model (where the collision rates are obtained from the fluid-derived quantities). In such a hybrid model, one only requires that the transport of the collision low-energy electrons be accurately represented by a fluid description since nonequilibrium processes are handled by the kinetic portion of the model.

We have developed a hybrid model for rf discharges that combines an electron Monte Carlo simulation (EMCS) for the temporally and spatially varying EED with a self-consistent fluid model (SCFM) for the densities and electric field. Excitation rates and transport coefficients as a function of space and time are obtained from the EMCS. These values are then used in a neutral chemistry/transport model (NCTM) that predicts neutral species densities. Collision rates from both the EMCS and NCTM are then used to generate temporally and spatially dependent source and sink functions for charged particles that are used in the SCFM to obtain charge densities and the electric field. The electric field is then used in the EMCS to update the EED, and the process is iterated until the solution converges. This process of iterating between an EMCS and SCFM has been previously used in solving for the electric field and charge densities in a dc cathode fall.<sup>17,18</sup> Reactions involving excited states of the gases (e.g., Penning reactions, multistep ionization) and charge exchange reactions can significantly perturb the charge balance in low-pressure plasmas. These reactions have therefore also been included in our hybrid model.

The advantage of using this technique in rf discharges is that the hybrid model may execute faster than either a kinetic model or a fluid model. Poisson’s equation is not solved during the EMCS portion of the hybrid model. Therefore, the number of particles needed to obtain statistically acceptable electron collision rates is only  $\approx 0.002$ – $0.01$  of that typically used in a PIC simulation where the statistics must be sufficient to solve Poisson’s equation. The EMCS portion of the hybrid model therefore executes 100–500 times more rapidly than a PIC simulation. We also note that it is not necessary to solve the energy equation within the fluid portion of the hybrid because transport and rate coefficients are provided by the EMCS. Since the energy equation tends to be the stiffest of the traditional fluid equations, its elimination speeds the SCFM. Therefore, the fluid portion of a hybrid model can execute faster than a fluid model that includes higher-order moments of Boltzmann’s equation.

The hybrid model will be described in detail in Sec. II. In Sec. III we present results from the hybrid model for rf

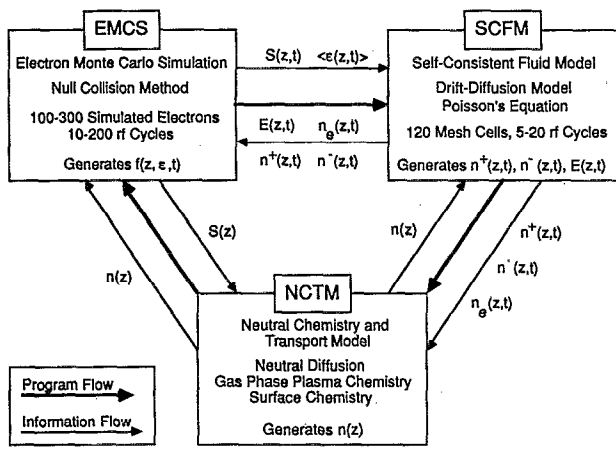


FIG. 1. Schematic of the hybrid model.  $n^+$ ,  $n^-$ ,  $n$ , and  $n_e$  are the densities of positive ions, negative ions, neutral species, and electrons, respectively.  $S$  represents production and loss rates, and  $\langle \epsilon \rangle$  is the mean electron energy. The bold arrows show the iterative flow of the computer program. The other arrows show the exchange of information.

discharges in the pure gases He, N<sub>2</sub>, and O<sub>2</sub>. These gases are representative of electropositive discharges in atomic and molecular electropositive gases, and of discharges in electronegative gases. In Sec. IV, we discuss results from the model for rf discharges in gas mixtures. The mixtures are for an air-contaminated He discharge (He/N<sub>2</sub>/O<sub>2</sub>), a He/CF<sub>4</sub>/O<sub>2</sub> discharge, and a Si<sub>3</sub>N<sub>4</sub> deposition gas mixture (SiH<sub>4</sub>/NH<sub>3</sub>). In this section we also present results from a companion plasma chemistry/flow model for the SiH<sub>4</sub>/NH<sub>3</sub> mixtures. Our concluding remarks are in Sec. V.

## II. DESCRIPTION OF THE MODEL

The mechanics of the hybrid model are schematically shown in Fig. 1. Initial estimates are made for the time- and space-averaged electron density  $\bar{n}_e$  and electric field  $E$  as a function of position  $z$  and phase  $\phi$ . (We use  $\phi$  to denote the time variable to emphasize the periodic nature of an rf discharge. Time-averaged quantities are to be understood as averaged over one rf cycle.) The electron Monte Carlo simulation (EMCS) is then executed using 100–500 pseudoparticles for 10–200 rf cycles. The resulting electron energy distribution (EED)  $f(z, \epsilon, \phi)$  is used to generate electron impact rate coefficients, source terms for electrons and ions, and transport coefficients, all as a function of position and phase. (The electron kinetic energy is  $\epsilon$ .) A neutral chemistry/transport model (NCTM) is used to obtain steady-state densities of minor neutral species, and associated source and sink rates for charged species. The source/sink terms and transport coefficients for all charged species are then passed to the self-consistent fluid model (SCFM). The SCFM is then run for 5–20 rf cycles, generating the density of all charged species  $n_j(z, \phi)$  and the electric field  $E(z, \phi)$ . The SCFM includes the pertinent plasma chemical reactions involving charged species, such as charge exchange. The EMCS is then executed with the updated neutral and ion densities, electron density  $\bar{n}_e$ , and electric field. This process is iterated for hundreds to thousands of rf cycles (as dictated by the time scale for physical

processes in the plasma) until the solution converges to a periodic steady state. The convergence criterion is based on the time rate of change of  $\bar{n}_e$  and is discussed below.

### A. Self-consistent fluid model

The self-consistent fluid model generates the densities of charged particles and the electric field as a function of position and phase in the rf discharge. The density  $n_j$  for each specie  $j$  is obtained in one spatial dimension  $z$  from the continuity equation,

$$\frac{\partial n_j}{\partial t} = -\frac{\partial}{\partial z} \left( v_j n_j - D_j \frac{\partial n_j}{\partial z} \right) + S_j - n_j \sum_i \kappa_{ij} n_i + \sum_{i,k} \kappa_{ijk} n_i n_j \quad (1)$$

(Note that we have suppressed the index denoting the spatial location.)  $S_j$  is the source term (from the EMCS) for charged species  $j$  resulting from electron impact processes (ionization, attachment, detachment, or recombination) with ground state neutrals, excited neutrals, and other charged species.  $S_j$  therefore reflects the full nonequilibrium nature of the EED. The drift velocity for specie  $j$  is  $v_j$  and  $D_j$  is its diffusion coefficient. The last two terms of Eq. (1) represent gas phase plasma-chemical reactions between heavy particles (ion-neutral, neutral-neutral) that either deplete or produce charged species  $j$ . The rate coefficient for collisions between species  $i$  and  $j$  producing charged species  $k$  is  $\kappa_{ijk}$ . This latter type of reaction includes charge exchange, ion-ion neutralization, Penning ionizations, and association collisions. The mechanics of data entry and execution for the entire nonelectron impact reaction scheme is completely general and is similar to that used for the CHEMKIN high-temperature combustion chemistry codes,<sup>26</sup> but it is tailored to address the low gas temperature gas phase chemistry of interest.

Tabulated mobilities<sup>27</sup> as a function of the reduced electric field  $E/N$  are used for the ions or generated from estimated constant cross sections if otherwise unavailable. All such mobilities are contained in a database that is queried during initialization given the gas species to be included in the model. The electron mobility during a particular iteration of the SCFM is found from the collision frequency  $\nu(z, \phi)$  generated in the previous EMCS iteration. The mobilities of electrons in the SCFM are obtained by determining the best fit parameters  $A$  and  $B$  in the expression

$$\ln \mu(z, \phi) = \ln \frac{q}{m\nu(z, \phi)} = A \ln E(z, \phi) + \ln B \quad (2)$$

for all discrete values of  $z$  and  $\phi$  in the EMCS electron statistics array. The expression  $\mu(E) = BE^A$  is then used to calculate the electron mobility in the SCFM until the next update by the EMCS. This fitting technique prevents statistical noise in the EMCS from producing artificial local extrema in the electron mobility that are numerically unstable. The electron mobility is, in general, well-represented by Eq. (2) with the exception of gases having deep Ramsauer cross sections in the range of interest. In that case, higher-order fits can be used. Diffusion coefficients

$D_j$  are obtained using these electron and ion mobilities and the Einstein relation  $D_j = \mu_j k_B T_j$ . The temperature  $T_j$  for the ions is assumed constant and equal to the neutral gas temperature (300 K here). The electron temperature and mobility are obtained from the EMCS and are functions of position and phase. [The electron temperature is  $2\langle\epsilon\rangle/3$ , where  $\langle\epsilon\rangle$  is the mean energy found by integrating over the distribution function  $f(z, \epsilon, t)$ .] The electric field that is used to determine the ion velocity at a particular spatial location is averaged over the response time of the ion. This technique prevents the relatively heavy ions from unphysically responding to the rapidly varying rf electric field.

The continuity equations for charged species in the SCFM are couched in finite difference form using the donor cell method. For a constant mesh spacing  $\Delta z$  the advective term is represented by

$$\frac{\partial n_{ji}}{\partial t} = - \left| \frac{v_{ji} n_{ji}}{\Delta z} \right| + \frac{1}{2\Delta z} (\{ |v_{j,i-1} n_{j,i-1}| + v_{j,i-1} n_{j,i-1} \} + \{ |v_{j,i+1} n_{j,i+1}| - v_{j,i+1} n_{j,i+1} \}), \quad (3)$$

where  $n_{ji}$  is the density of species  $j$  at mesh point  $i$ , and the drift velocities  $v_{ji}$  are evaluated at cell centers. This formulation is used because it is second-order accurate and will vectorize.

The transport equations, electron source terms, and Poisson's equation are directly integrated using the Euler method. The kinetic terms to the continuity equation [the last two terms in Eq. (1)] are separately included after the transport update using a time slicing technique. The time step is dynamically chosen after every ten SCFM updates to satisfy the Courant limit  $\Delta t < \min(\Delta z/v_{ji})$  for all species  $j$  and spatial locations  $i$ . We typically limit  $\Delta t < 0.3 \min(\Delta z/v_{ji})$ . The time step is also limited in a self-consistent local field approximation model by the stiffness of Poisson's equation:<sup>25,28</sup>

$$\Delta t < \min \left( \epsilon_0 / \left[ e \sum_j n_{ji} t_{ji} \right] \right), \quad (4)$$

again for species  $j$  at location  $i$  with density  $n_{ji}$  and mobility  $\mu_{ji}$ . The permittivity of free space is  $\epsilon_0$ , and  $e$  is the unit charge ( $e > 0$ ). To guarantee stability,  $\Delta t$  is typically limited to 0.5 of that specified by Eq. (4). With these limits, the time step is typically  $5 \times 10^{-13} < \Delta t < 1 \times 10^{-11}$  s.

For discharges at low pressures and high plasma densities, Eq. (4) becomes a rather burdensome limit. In these cases, the electric field in the SCFM can be damped to allow stable integration for a time step  $\approx 5$  times larger than that specified by Eq. (4). Let  $E(z, t)$  be the field that was most recently obtained from Poisson's equation using the instantaneous charge densities. Instead of using  $E(z, t)$  as the basis of the next fluid time step, we can use a weighted average of the field, which we denote as  $E'(z, t)$ . This weighted average is obtained from  $E(z, t)$  and the field at the previous time step;  $E'(z, t) = fE(z, t) + (1 - f)E'(z, t - \Delta t)$ . Since  $E'(z, t - \Delta t)$  was also found using the same weighting scheme,  $E'(z, t)$  contains information from all past times. Typically, stable conditions are obtained using  $0.2 < f < 0.4$ . (Note that if  $f = 1$ , one recovers

the undamped solution.) Since one must operate at a smaller fraction of the Courant limit when using the damped field scheme [ $\Delta t < 0.1 \min(\Delta z/v_{ji})$ ] the method is only useful when the Courant limit (plasma flow) is not the more restrictive factor in the integration.

## B. The electron Monte Carlo simulation

The EMCS is functionally similar to that described in Ref. 21 and so it will be only briefly described with emphasis on improvements to the previously reported model. A major improvement has been making the EMCS completely general with respect to gas composition. Based on the gas species that are specified to be included in the model, the required electron impact cross sections, anisotropic scattering factors, and parameters for the distribution of secondary electrons produced during ionizations are extracted from a database. These parameters are entered into lookup tables for later use.

The electric field  $E(z, \phi)$  is known at the beginning of any given run of the EMCS, either by assuming it at the very start of the hybrid model or later by calculating it in the SCFM. The electric fields are interpolated onto a two-dimensional array for position and phase during the rf cycle having a fine mesh of equal spacing in either position or phase. When the electric field is required during the EMCS, this array is interpolated for position and phase. The even spacing of the mesh affords rapid lookups during the EMCS and the storage requirements are nominal. The simulated electrons (typically 100–500) are initially randomly distributed between the electrodes with velocities randomly selected from a Maxwellian having a temperature of 1 eV. On subsequent iterations when the EMCS uses the updated  $E(z, \phi)$  from the SCFM, the initial conditions for the particles are obtained from the locations and trajectories of particles from the previous iteration of the EMCS.

The electron energy distribution  $f(z, \epsilon, \phi)$  in the EMCS is formed by periodically recording the phase space location of each electron  $(z, \epsilon, \phi)$ , where  $z$  is the distance between the electrodes,  $\epsilon$  is the kinetic energy of the electron, and  $\phi$  is the phase of the rf cycle. Numerically,  $f$  is an array known on a discrete volume of phase space  $\Delta z_i \Delta \epsilon_j \Delta \phi_k$  centered on  $z_i$ ,  $\epsilon_j$ , and  $\phi_k$ . Collecting statistics involves determining the  $(z_i, \epsilon_j, \phi_k)$  bin that contains the phase space location of each electron and then incrementing  $f(z_i, \epsilon_j, \phi_k)$  by an appropriate amount.

Two methods have been used to gather statistics from the pseudoparticles and form the electron energy distribution. In both methods, the trajectories of individual electron particles are integrated in time with time steps given by the minimum of the randomly selected time to the next collision, 0.01 of the rf cycle, or the time required to transverse 0.02 of the sheath or 0.01 of the interelectrode spacing. In doing so, individual electron particles find themselves at different phases in the rf cycle.

In the first method of gathering statistics, the particles are moved forward in time until they reach the next specified phase at which statistics are to be gathered. Particles

arriving at this phase are not moved while they wait for the slower particles to catch up. When all particles have reached the recording phase, statistics are recorded, and the particles once again diverge in phase as their trajectories are again integrated with different time steps. Statistics are typically accumulated at fixed 2 ns intervals during the EMCS.

The second method for gathering statistics is similar to that just described, but statistics for each electron are recorded after every time step. The incremental value added to  $f(z, \epsilon, \phi_i)$  is weighted by the previous time step (which is different for each electron). This method is less flexible, but can be used to minimize statistical noise at the cost of a somewhat greater computational effort.

Ionization, attachment, and loss of electrons to the electrodes can change the number of pseudoparticles in the EMCS. When the number of pseudoparticles has increased or decreased by predetermined amounts, simulated electrons are removed or added (in a statistically unbiased fashion) to the EMCS to maintain approximately the same number of simulated particles. This "renormalization" becomes less frequent as the calculation proceeds away from the arbitrary initial conditions and toward the final periodic steady-state solution.

Electron collisions within the EMCS are implemented using the efficient "null collision" algorithm.<sup>29,30</sup> Use of a modified version of the null collision algorithm allows electron collisions with species whose densities evolve during the simulation to be easily included. Densities of major fill gas species are fixed throughout the hybrid calculation, and minor species densities ( $< 10^{-4}$  of the fill gas density) are known, either initially by assumption or later from the SCFM and NCTM. The electron kinetic energy range of interest is divided into a selected number of ranges. Each range  $k$  is divided into energy bins  $j$  centered on  $\epsilon_{jk}$ . The width of the energy bins in each range is chosen to resolve any structure in the cross sections or structure expected in the EED. The total electron collision frequency in each energy interval  $\nu_i$  (sequentially indexed from low to high electron energy) is determined and probability arrays are initialized for each energy interval. The probability arrays are denoted  $P_{ij}$  for energy  $i$  and collision process  $j$  and are constructed such that

$$P_{ij} = \frac{\nu'_{ij}}{\nu_i}, \quad \nu'_i = \sum_{l=1, j} \nu_{il} \quad (5)$$

where  $\nu_{ij}$  is the collision frequency for energy interval  $i$  and process  $j$ ,  $\nu'_i$  is the cumulative collision frequency for processes  $l < j$ , and  $P_{ij}$  is normalized so that for  $m$  processes,  $P_{im} = 1$ . A null or self-scattering cross section is added to each energy interval so that the total (and maximum) collision frequency  $\nu^{\max}$ , including the null portion, is constant over a given energy range. (Here we suppress the index denoting the subrange.) The null collision process at energy  $\epsilon_i$  has collision frequency  $\nu^{\text{null}}(\epsilon_i) = \nu_i^{\text{null}} = \nu^{\max} - \sum_j \nu_j(\epsilon_i)$ , where the sum is over the collision process  $j$ . Using the Monte Carlo method, the time to the next collision is obtained from  $\Delta t = -\ln(r_1)/\nu^{\max}$ , where  $r_1$  is the first in a sequence of random numbers that are uniformly

distributed on  $[0, 1]$ . After updating the velocity and location of the particle using this time step, another random number is chosen. If  $r_2 > \nu_i^{\text{null}}/\nu^{\max}$ , where the energy bin  $i$  is based on the instantaneous energy of the electron, then a real collision has occurred, and the particle velocity is revised accordingly. The specific collision that occurs is obtained by using  $r_2$  to find the collision that satisfies

$$P_{i, j-1} < r_2 \leq P_{i, j} \quad (6)$$

If  $r_2 < \nu_i^{\text{null}}/\nu^{\max}$ , then a "null" collision occurs and the particle proceeds unhindered (that is, without changing its phase space coordinates) to its next possible collision.

The energy-resolved electron collision frequencies change during the simulation due to the changes in the density of charged and excited state densities. A modified null collision technique is used to avoid unnecessary recalculation of the collision probability arrays. The probability arrays described above are initialized using the electron impact cross sections for all ground state, excited species, ions, and reaction products of interest. The densities of all of these species vary throughout the calculation and are not initially known. The collision frequencies are therefore calculated using the maximum expected density of each species  $i$ ,  $n_i^{\max}$ .  $n_i^{\max}$  is known and fixed for the feedstock gases, but  $n_i^{\max}$  must be estimated for all species whose density evolves during the simulation. If during the simulation a collision with species  $i$  is selected at spatial location  $z$ , another random number  $r_3$  is selected. If  $r_3 < n_i(z)/n_i^{\max}$ , a real collision takes place and the collision algorithms are invoked. If  $r_3 > n_i(z)/n_i^{\max}$ , then the collision is "null" and the particle proceeds unhindered. This method whereby the null collision probability is not constant is reminiscent of that employed by Weng and Kushner<sup>31</sup> in a study of electron-electron collisions in gas discharges.

### C. The neutral chemistry and transport model

Three disparate time scales must be addressed in the rf discharges of interest. The shortest time scale is that for electron transport, the intermediate is that for ion transport, and the longest is that for neutral transport. The disparity between the time scales for electron and ion transport is the limiting factor in typical hydrodynamic and kinetic simulations of rf discharges. Many techniques have been introduced to speed execution of models, such as advancing the ions less frequently but using an appropriately longer time step than that for the electrons. We have chosen not to incorporate any such algorithms since the EMCS and SCFM execute acceptably rapidly. We have, however, capitalized on the condition that the transport of neutral particles has time scales that span perhaps  $10^4$  rf cycles. The excitation rate coefficients that influence the density of these species are well represented by spatially dependent, time-averaged values. These neutral species densities are obtained from the neutral chemistry/transport model (NCTM) after executing the EMCS and before the SCFM during each iteration of the hybrid model. The mechanics of the NCTM are as follows.

After executing the EMCS, one has the electron impact rate coefficients for all processes  $i$  as a function of

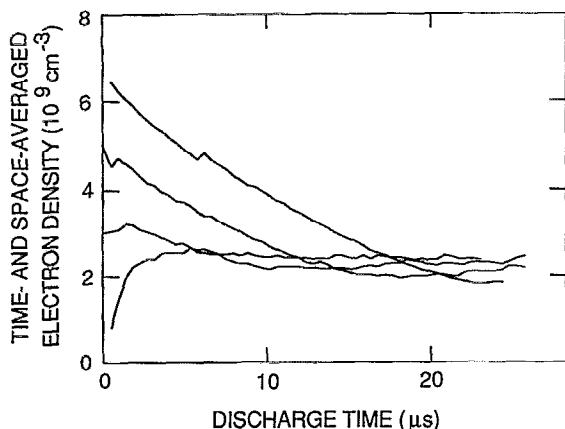


FIG. 2. Convergence of time- and space-averaged electron density  $\bar{n}_e$  for  $\text{SiH}_4/\text{NH}_3 = 0.1/0.9$  gas mixture for various initial estimates for  $\bar{n}_e$ .

position and phase in the rf cycle  $\kappa_i(z, \phi)$ . These coefficients are averaged over the rf cycle to obtain excitation rates as a function of position  $\kappa_i(z)$ . These rate coefficients are then used to formulate the continuity equation for each neutral species:

$$\frac{\partial n_{im}}{\partial t} = D_{im} \frac{\partial^2}{\partial z^2} (D_{im} n_{im}) - n_{im} S_{im}^0 + S_{im}^1 \quad (7a)$$

$$S_{im}^0 = \sum_j \kappa_{jim} n_{jm}, \quad S_{im}^1 = \sum_{j,k} \kappa_{jkm}^i n_{jm} n_{km} \quad (7b)$$

In Eqs. (7),  $n_{im}$  is the density of species  $i$  at location  $m$ ,  $\kappa_{jim}$  is the rate coefficient for collision of species  $i$  with  $j$  at location  $m$ , and  $\kappa_{jkm}^i$  is the rate coefficient for collisions of species  $j$  and  $k$  producing species  $i$  as a product at location  $m$ .  $S_{im}^1$  therefore represents the source function for species  $i$  (including electron collision process) at location  $m$  and  $n_{im} S_{im}^0$  represents the "sink" function.

The steady-state spatial distribution of species  $i$  can quickly be obtained by expressing Eq. (7) in finite difference form

$$n_{im} = \frac{(n_{i,m+1} + n_{i,m-1}) + [S_{im}^1 / (\Delta z^2 / D_i)]}{(1 + \beta_i) + [S_{im}^0 / (\Delta z^2 / 2D_i)]}, \quad (8)$$

where, for presentation purposes here, we have used a constant mesh size and diffusion coefficient.  $\beta_i$  is the destructive reactive sticking coefficient for species on the electrodes. For computational cells away from the boundary  $\beta_i = 1$ . Contributions to  $n_{im}$  by surface processes (for example,  $\text{He}^+ \rightarrow \text{wall} \rightarrow \text{He}$ ) are incorporated into  $S_{im}^1$ . By assuming that  $S_{im}^1$  and  $S_{im}^0$  can be independently specified, Eq. (8) can be represented by a tridiagonal matrix operator, and  $n_{im}$  can be efficiently determined using matrix inversion.

In some cases the factors  $S_{im}^1$  and  $S_{im}^0$  may themselves be functions of the species densities. The solution of Eq. (8) for all species is therefore iterated, recomputing  $S_{im}^1$  and  $S_{im}^0$  after each successive estimate for  $n_{im}$ . Tens to hundreds of iterations are typically required for all densities to converge to better than  $5 \times 10^{-6}$  between iterations.

More iterations are required when  $S^1$  and  $S^0$  have highly nonlinear terms such as for Penning ionizations. We have no formal proof that this iteration procedure will necessarily converge, although in practice it always does. It is also not obvious that solving for the steady-state neutral densities after each call to the EMCS will necessarily result in convergence of the overall hybrid model iteration technique, but in practice the method does converge in a physically realistic manner. The iterated matrix inversion method is computationally faster than any time integration technique we investigated, and it consumes a negligible amount of computer time compared to the remainder of the hybrid calculation.

#### D. Companion plasma chemistry model

Many neutral species are produced having densities that are sufficiently low that they do not significantly affect electron and ion transport, yet are quite important to the deposition or etching process. For example,  $\text{NH}_2$  and  $\text{SiH}_3$  radicals are generated in discharges sustained in  $\text{SiH}_4/\text{NH}_3$  mixtures for  $\text{Si}_3\text{N}_4$  deposition. If the feedstock gases are not heavily dissociated, the radical densities may not be important to electron transport. In these cases, the source functions  $S^1$  and  $S^0$  resulting from electron impact processes can be used in a separate plasma chemistry model in which the reaction scheme can be arbitrarily complex without affecting the execution speed of the hybrid model.

We have followed such a strategy in cases where it is appropriate. The electron impact source functions  $S^1$  and

TABLE I. Summary of conditions for hybrid model results presented in this article.

Gas mixture	Gas pressure (Torr)	rf voltage amplitudes at discharge (V)	Electrode gap (cm)	Comment
He	0.5	75	2.54	Both with
He	0.5	100	2.54	and without
He	0.5	150	2.54	metastable
He	1.0	75	2.54	He
He	1.0	100	2.54	
He	1.0	150	2.54	
He	1.0	200	2.54	
N <sub>2</sub>	1.0	150	2.54	
N <sub>2</sub>	1.0	200	2.54	
N <sub>2</sub>	1.0	300	2.54	
N <sub>2</sub>	1.0	400	2.54	
N <sub>2</sub>	1.0	500	2.54	
O <sub>2</sub>	0.25	200	1.6	
O <sub>2</sub>	0.5	200	1.6	
O <sub>2</sub>	1.0	200	1.6	
O <sub>2</sub>	2.0	200	1.6	
He/N <sub>2</sub> /O <sub>2</sub>	0.5	150	2.54	He contaminated by dry air
				$= 0.9999/8 \times 10^{-5}/2 \times 10^{-5}$
He/CF <sub>4</sub> /O <sub>2</sub>				
				$= 0.90/0.05/0.05$
SiH <sub>4</sub> /NH <sub>3</sub> = 0.01/0.99	0.2	200	2.54	
SiH <sub>4</sub> /NH <sub>3</sub> = 0.03/0.97	0.2	200	2.54	
SiH <sub>4</sub> /NH <sub>3</sub> = 0.1/0.9	0.2	200	2.54	
SiH <sub>4</sub> /NH <sub>3</sub> = 0.2/0.8	0.2	200	2.54	
SiH <sub>4</sub> /NH <sub>3</sub> = 0.3/0.7	0.2	200	2.54	
SiH <sub>4</sub> /NH <sub>3</sub> = 0.4/0.6	0.2	200	2.54	

$S^0$  were exported to a plasma chemistry that is functionally similar to that described in Ref. 32, and species densities as a function of position were computed. Enhancements to that plasma chemistry model have been made and will be described in an upcoming publication in the context of remote plasma enhanced chemical vapor deposition.<sup>33</sup>

### E. Convergence criterion and timings

A particular run of the hybrid model is declared converged when the absolute fractional change per rf cycle of  $\bar{n}_e$ , the time- and space-averaged electron density, is less than  $3 \times 10^{-4}$  per rf cycle for 10 calls to the SCFM, and that this criterion is met for five successive calls of the SCFM. This method ensures that statistical noise and local extrema (in time) of  $\bar{n}_e$  do not falsely signal convergence. Convergence to a single solution independent of the initial conditions was tested by starting otherwise identical runs with different initial values of  $\bar{n}_e$  and verifying that they did indeed converge to the same answer (Fig. 2).

We have chosen to demonstrate the convergence criterion in a gas mixture with rather complex gas phase chemistry ( $\text{SiH}_4/\text{NH}_3$ ) to indicate that convergence based on  $\bar{n}_e$  is sufficient to ensure convergence of other discharge quantities. Convergence time is dictated by the physical processes in the discharge plasma and is typically hundreds of rf cycles at low pressure (hundreds of mTorr) and thousands of rf cycles at higher pressure (several Torr).

We typically collect EMCS statistics from 100–500 simulated electrons for 10–200 rf cycles. The transport coefficients and source functions obtained from the EED have an acceptably small amount of noise ( $< 5\%$  statistical variation). The SCFM is run for 5–20 rf cycles during each iteration of the hybrid model. Monte Carlo simulations are, in general, not vectorizable, but the SCFM is highly vectorized. In spite of this, the nonvectorizable portion of the code (the EMCS and NCTM) usually constitutes  $< 10\%$  of the total execution time. A single case starting with an arbitrary value of  $\bar{n}_e$  typically requires 0.5–20 h on a laboratory minicomputer (Stardent 3000) which has vector capability. This corresponds to a physical discharge time of tens to many hundreds of  $\mu\text{s}$ , or up to 5000 rf cycles at 13.56 MHz.

### III. SIMULATED rf DISCHARGES HAVING A SINGLE FILL GAS

In this section we present a sampling of results from the hybrid model for discharges in a noble gas (He), an electropositive molecular gas ( $\text{N}_2$ ), and an electronegative gas ( $\text{O}_2$ ). Table I summarizes all of the discharge conditions presented in this article. The electron impact and plasma chemical processes included in the model are listed in Table II. All cases discussed in this article are for a rf frequency of 13.56 MHz. All voltages are specified as amplitudes of the applied sinusoidal rf potential.

TABLE II. Reactions and rates included in the hybrid model.

Process	Where included <sup>a</sup>	Rate or rate coefficient <sup>b</sup>	Reference
<b>He discharges</b>			
$e + \text{He} \rightarrow e + \text{He}$	EMCS	c	37
$e + \text{He} \rightarrow e + \text{He}^*$	EMCS, NCTM <sup>e</sup>	c	38
$e + \text{He} \rightarrow e + \text{He}^{**}$	EMCS, NCTM <sup>e</sup>	c	38
$e + \text{He} \rightarrow e + e + \text{He}^+$	EMCS, SCFS <sup>e</sup>	c	39
$e + \text{He}^* \rightarrow e + \text{He}^{**}$	EMCS, NCTM <sup>e</sup>	c	40
$e + \text{He}^* \rightarrow e + \text{He}$	EMCS, NCTM <sup>e</sup>	c	d
$e + \text{He}^* \rightarrow e + e + \text{He}^+$	EMCS, NCTM, SCFM <sup>e</sup>	c	41
$e + \text{He}^{**} \rightarrow e + e + \text{He}^+$	EMCS, NCTM, SCFM <sup>e</sup>	c	41
$e + \text{He}^+ \rightarrow e + \text{He}^+$	EMCS	c	42
$e + \text{He}^+ \rightarrow e + \text{He}^*$	EMCS, NCTM, SCFM <sup>e</sup>	c	43
$\text{He}^* + \text{He}^* \rightarrow \text{He} + \text{He}^+ + e$	NCTM, SCFM	1.5 (–9)	44
$\text{He}^* + \text{He} \rightarrow \text{He} + \text{He}$	NCTM	5.8 (–15)	45
<b>N<sub>2</sub> discharges</b>			
$e + \text{N}_2 \rightarrow e + \text{N}_2$	EMCS	c	37
$e + \text{N}_2 \rightarrow e + \text{N}_2(r)$	EMCS	c	46
$e + \text{N}_2(v=0) \rightarrow e + \text{N}_2(v=n), n=1,8$	EMCS, NCTM <sup>f</sup>	c	47
$e + \text{N}_2 \rightarrow e + \text{N}_2(A^3\Sigma)$	EMCS, NCTM <sup>f</sup>	c	$< 18$ eV, 48 $> 18$ eV, 49
$e + \text{N}_2 \rightarrow e + \text{N}_2(B^3\Pi, W^3\Delta)$	EMCS, NCTM <sup>f</sup>	c	$< 14$ eV, 50 $> 14$ eV, 49
$e + \text{N}_2 \rightarrow e + \text{N}_2(B^3\Sigma)$	EMCS, NCTM <sup>f</sup>	c	51
$e + \text{N}_2 \rightarrow e + \text{N}_2(a^1\Sigma, a''\Pi, w^1\Delta)$	EMCS, NCTM <sup>f</sup>	c	51
$e + \text{N}_2 \rightarrow e + \text{N}_2(C^3\Pi, E^3\Sigma, a''^1\Sigma)$	EMCS, NCTM <sup>f</sup>	c	51
$e + \text{N}_2 \rightarrow e + 2\text{N}$	EMCS, NCTM	c	51
$e + \text{N}_2 \rightarrow e + e + \text{N}_2^+$	EMCS, SCFM	c	39
$e + \text{N}_2(v) \rightarrow e + \text{N}_2(v)$	EMCS <sup>f</sup>	c	37
$e + \text{N}_2(v) \rightarrow e + \text{N}_2$	EMCS, NCTM <sup>f</sup>	c	N <sub>2</sub> analogy d
$e + \text{N}_2(v) \rightarrow e + \text{N}_2^*$	EMCS, NCTM <sup>f</sup>	c	51
			N <sub>2</sub> analogy

TABLE II. (Continued.)

Process	Where included <sup>a</sup>	Rate or rate coefficient <sup>b</sup>	Reference
$e + N_2(v) \rightarrow e + e + N_2^+$	EMCS, NCTM, SCFM <sup>f</sup>	c	39
$e + N_2^* \rightarrow e + N_2^*$	EMCS <sup>f</sup>	c	51
$e + N_2^* \rightarrow e + N_2(v)$	EMCS, NCTM <sup>f</sup>	c	N <sub>2</sub> analogy d
$e + N_2^* \rightarrow e + N_2$	EMCS, NCTM <sup>f</sup>	c	d
$e + N_2^* \rightarrow e + N_2^+$	EMCS, NCTM, SCFM <sup>f</sup>	c	41
$e + N_2^+ \rightarrow e + N_2^+$	EMCS	c	42
$e + N_2^+ \rightarrow 2N$	EMCS, NCTM, SCFM	c	52
$e + N_4^+ \rightarrow e + N_4^+$	EMCS	c	42
$e + N_4^+ \rightarrow N_2 + N_2$	EMCS, NCTM, SCFM	c	52; scaled
$e + N^+ \rightarrow e + N^+$	EMCS	c	42
$e + N^+ \rightarrow N$	EMCS, NCTM, SCFM	c	43
$N_2^* + N_2^* \rightarrow N_2^* + N_2$	NCTM	1.36(-9)	53
$N_2^* + N_2 \rightarrow N_2 + N_2$	NCTM	1.9(-13)	54
$N_2^+ + N_2 + N_2 \rightarrow N_4^+ + N_2$	SCFM	1.9(-29) cm <sup>6</sup> s <sup>-1</sup>	55
$N_2(v) + N_2(v) \rightarrow N_2 + N_2(v)$	NCTM	1.0(-12)	f
$N_2(v) + N_2 \rightarrow N_2 + N_2$	NCTM	3.0(-22)	f
<b>O<sub>2</sub> discharges</b>			
$e + O_2 \rightarrow e + O_2$	EMCS	c	56
$e + O_2 \rightarrow e + O + O^-$	EMCS, SCFM	c	56
$e + O_2 \rightarrow e + O_2(r)$	EMCS	c	56
$e + O_2 \rightarrow e + O_2(v=n), n=1,6$	EMCS	c	56
$e + O_2 \rightarrow e + O_2(^1D)$	EMCS, NCTM <sup>g</sup>	c	56
$e + O_2 \rightarrow e + O_2(B^1S)$	EMCS, NCTM <sup>g</sup>	c	56
$e + O_2 \rightarrow e + O_2^*(4.5 eV)$	EMCS, NCTM <sup>g</sup>	c	56
$e + O_2 \rightarrow e + O_2^*(6 eV)$	EMCS, NCTM <sup>g</sup>	c	56
$e + O_2 \rightarrow e + 2 \cdot O(8.4 eV)$	EMCS, NCTM	c	56
$e + O_2 \rightarrow e + 2 \cdot O(10 eV)$	EMCS, NCTM	c	56
$e + O_2 \rightarrow e + e + O_2^+$	EMCS, SCFM	c	56
$e + O_2^+ \rightarrow e + O_2^+$	EMCS	c	42
$e + O_2^+ \rightarrow O + O$	EMCS, NCTM	c	52
$O_2^+ + O^- \rightarrow O_2 + O$	NCTM, SCFM	1.0(-7)	57
$O^+ + O^- \rightarrow O + O$	NCTM, SCFM	2.7(-7)	57
$O^+ + O_2 \rightarrow O_2^+ + O$	NCTM, SCFM	1.9(-11)	55
$O_2^+ + O_2^- \rightarrow O_2 + O_2$	NCTM, SCFM	4.2(-7)	57
$O^+ + O_2^- \rightarrow O + O_2$	NCTM, SCFM	1.0(-7)	h
$O^- + O \rightarrow O_2 + e$	NCTM, SCFM	3.0(-10)	58
$e + O_2 + O_2 \rightarrow O_2 + O_2^-$	SCFM	1.5(-30) cm <sup>6</sup> s <sup>-1</sup>	59
<b>He/N<sub>2</sub>/O<sub>2</sub> discharges</b>			
All reactions for He, N <sub>2</sub> , and O <sub>2</sub> , plus the following:			
$N_2^+ + N_2 + He \rightarrow N_4^+ + He$	NCTM, SCFM	1.9(-29)	55
$He^+ + O_2 \rightarrow He + O^+ + O$	NCTM, SCFM	1.0(-9)	55
$He^+ + N_2 \rightarrow He + N_2^+$	NCTM, SCFM	5.0(-10)	55
$He^+ + N_2 \rightarrow He + N^+ + N$	NCTM, SCFM	7.0(-10)	55
$He^+ + N_2(v) \rightarrow He + N_2^+$	NCTM, SCFM	5.0(-10)	55
$He^+ + N_2(v) \rightarrow He + N^+ + N$	NCTM, SCFM	7.0(-10)	55
$N_2^+ + O_2 \rightarrow N_2 + O_2^+$	NCTM, SCFM	5.0(-11)	55
$He^* + O_2 \rightarrow O_2^+ + He + e$	NCTM, SCFM	2.5(-10)	60
$He^* + N_2 \rightarrow N_2^+ + He + e$	NCTM, SCFM	7.0(-11)	60
$He^* + N_2(v) \rightarrow N_2^+ + He + e$	NCTM, SCFM	7.0(-11)	60
<b>N<sub>2</sub> analogy</b>			
$N_2^* + O_2 \rightarrow N_2 + O_2$	NCTM, SCFM	2.8(-12)	54
$N^+ + O_2 \rightarrow O_2^+ + N$	NCTM, SCFM	4.0(-10)	55
$N_4^+ + O_2 \rightarrow O_2^+ + N_2 + N_2$	NCTM, SCFM	2.5(-10)	55
$He^+ + O_2^- \rightarrow He + O_2$	NCTM, SCFM	5.0(-8)	55
$He^+ + O^- \rightarrow He + O$	NCTM, SCFM	5.0(-8)	i
$N_2^+ + O_2^- \rightarrow N_2 + O_2$	NCTM, SCFM	5.0(-8)	i
$N_2^+ + O^- \rightarrow N_2 + O_2$	NCTM, SCFM	5.0(-8)	i
$N^+ + O_2^- \rightarrow N + O_2$	NCTM, SCFM	5.0(-8)	i
$N^+ + O^- \rightarrow N + O$	NCTM, SCFM	5.0(-8)	i
<b>He/CF<sub>4</sub>/O<sub>2</sub> discharges</b>			
All reactions for He and O <sub>2</sub> , reactions from He/N <sub>2</sub> /O <sub>2</sub> involving He, O <sub>2</sub> , and their progeny, plus the following:			
$e + CF_4 \rightarrow e + CF_4$	EMCS	c	61

TABLE II. (Continued.)

Process	Where included <sup>a</sup>	Rate or rate coefficient <sup>b</sup>	Reference
$e + CF_4 \rightarrow e + CF_4(v2,4)$	EMCS	c	61
$e + CF_4 \rightarrow e + CF_4(v1,3)$	EMCS	c	61
$e + CF_4 \rightarrow CF_3 + F^-$	EMCS, NCTM, SCFM	c	61
$e + CF_4 \rightarrow e + CF_x + (4-x)F \rightarrow e + CF_x$	EMCS, NCTM	c	61
$e + CF_4 \rightarrow e + e + CF_3^+ + F$	EMCS, NCTM, SCFM	c	61
$He^* + CF_4 \rightarrow CF_3^+ + F + He + e$	NCTM, SCFM	1.0(-10)	62
$He^+ + CF_4 \rightarrow He + CF_3^+ + e$	SCFM	1.0(-9)	i
$CF_3^+ + F^- \rightarrow CF_3 + F$	SCFM	5.0(-8)	i
$F^- + He^+ \rightarrow F + He$	SCFM	5.0(-8)	i
$F^- + O_2^+ \rightarrow F + O_2$	SCFM	5.0(-8)	i
$F^- + O^+ \rightarrow F + O_2$	SCFM	5.0(-8)	i
$O^- + CF_3^+ \rightarrow O + CF_3$	SCFM	5.0(-8)	i
$O_2^- + CF_3^+ \rightarrow O_2 + CF_3$	SCFM	5.0(-8)	i
<b>SiH<sub>4</sub>/NH<sub>3</sub> discharges<sup>1</sup></b>			
$e + SiH_4 \rightarrow e + SiH_4$	EMCS	c	32 <sup>k</sup>
$e + SiH_4 \rightarrow e + SiH_4(v2,4)$	EMCS	c	32 <sup>k</sup>
$e + SiH_4 \rightarrow e + SiH_{(4-x)} + xH$	EMCS	c	32 <sup>k</sup>
$e + SiH_4 \rightarrow e + e + SiH_3^+$	EMCS, SCFM	c	32 <sup>k</sup>
$e + SiH_4 \rightarrow e + e + SiH_2^+$	EMCS, SCFM	c	32 <sup>k</sup>
$e + SiH_4 \rightarrow SiH_3^- + H$	EMCS, SCFM	c	32 <sup>k</sup>
$SiH_2^+ + SiH_4 \rightarrow SiH_3^+ + SiH_3$	SCFM	1.07(-9)	63
$SiH_x^+ + SiH_x^- \rightarrow SiH_4 + SiH_4$	SCFM	5.0(-8)	i
$e + NH_3 \rightarrow NH_3 + e$	EMCS	c	64
$e + NH_3 \rightarrow NH_3(v=n), n = 1,3$	EMCS	c	64
$e + NH_3 \rightarrow e + NH_2 + H$	EMCS	c	64
$e + NH_3 \rightarrow e + NH + 2H$	EMCS	c	64
$e + NH_3 \rightarrow NH_2 + H^-$	EMCS, SCFM	c	64
$NH_3^+ + SiH_x^- \rightarrow NH_3 + SiH_x$	SCFM	5.0(-8)	i
$NH_2^+ + SiH_x^- \rightarrow NH_3 + SiH_x$	SCFM	5.0(-8)	i
$SiH_x^+ + SiH_x^- \rightarrow SiH_4 + SiH_x$	SCFM	5.0(-8)	i
$NH_3^+ + SiH_4^- \rightarrow NH_3 + SiH_x$	SCFM	5.0(-8)	i
$NH_2^+ + SiH_x^- \rightarrow NH_3 + SiH_x$	SCFM	5.0(-8)	i
$NH_4^+ + SiH_x^- \rightarrow NH_3 + SiH_x$	SCFM	5.0(-8)	i
$SiH_x^+ + H^- \rightarrow SiH_4 + SiH_x$	SCFM	5.0(-8)	i
$NH_3^+ + H^- \rightarrow NH_3 + H$	SCFM	5.0(-8)	i
$NH_2^+ + H^- \rightarrow NH_3 + SiH_4$	SCFM	5.0(-8)	i
$NH_4^+ + H^- \rightarrow NH_3 + 2 \cdot H$	SCFM	5.0(-8)	i
$NH_3^+ + SiH_4^- \rightarrow NH_4^+ + SiH_3$	SCFM	2.64(-9)	65
$NH_2^+ + SiH_4^- \rightarrow NH_3 + SiH_3$	SCFM	9.54(-10)	65
$NH_3^+ + NH_3 \rightarrow NH_4^+ + NH_2$	SCFM	2.20(-9)	65
$NH_2^+ + NH_3 \rightarrow NH_3^+ + NH_2$	SCFM	1.0(-9)	33
$SiH_3^+ + NH_3 \rightarrow SiH_4N^+ + H_2$	SCFM	3.0(-10)	65
$SiH_2^+ + NH_3 \rightarrow NH_4^+ + SiH_2$	SCFM	2.5(-10)	65
$SiH_2^+ + NH_3 \rightarrow SiH_4N^+ + H$	SCFM	4.6(-10)	65
$SiH_2 + NH_3 \rightarrow SiH_3N^+ + H_2$	SCFM	1.3(-10)	65
$SiH_3N^+ + NH_3 \rightarrow SiH_4N^+ + H_2$	SCFM	6.36(-10)	65

<sup>a</sup>EMCS is the electron Monte Carlo simulation; SCFM is the self-consistent fluid model; NCTM is the neutral chemistry/transport model.

<sup>b</sup>1.0(-10)  $\equiv 1 \times 10^{-10}$ . Rate coefficients have units of  $cm^3 s^{-1}$  unless noted otherwise.

<sup>c</sup>Reaction rate found dynamically from cross section and calculated electron energy distribution from EMCS portion of the hybrid model.

<sup>d</sup>Cross section for superelastic process was obtained by detailed balance.

<sup>e</sup>He\* is a composite specie denoting all metastable electronically excited He atoms; He\*\* is a composite specie representing all radiating electronically excited He atoms in the NCTM.

<sup>f</sup>In the EMCS, we accounted for energy loss due to excitation to all vibrational states of N<sub>2</sub>. In the NCTM, a single vibrational state for N<sub>2</sub> was used. The rate of excitation to that state was the sum of excitation to N<sub>2</sub>( $v = n$ ),  $n = 1,8$ . Appropriately weighted cross sections for excitation, superelastic relaxation, and ionization of N<sub>2</sub>( $v$ ) were used in the EMCS. In a similar fashion, a single electronically excited state for N<sub>2</sub> was used in the NCTM. N<sub>2</sub><sup>\*</sup> is a composite species representing all electronically excited N<sub>2</sub> in the NCTM. Estimates for N<sub>2</sub>( $v$ ) heavy particle collisions were made by scaling rate coefficients found in S. K. Dhali, Trans. Plasma. Sci. 17, 603 (1989).

<sup>g</sup>A single excited state for O<sub>2</sub> (O<sub>2</sub><sup>\*</sup>) was used in the NCTM in a similar fashion as N<sub>2</sub>. See footnote above.

<sup>h</sup>By analogy to O<sub>2</sub><sup>+</sup> + O<sup>-</sup>  $\rightarrow$  O<sub>2</sub> + O.

<sup>i</sup>Estimate.

<sup>j</sup>Full plasma chemistry reaction scheme is included in coupled model. See text and Ref. 33.

<sup>k</sup>Cross-section set for SiH<sub>4</sub> was compiled from a variety of sources, and is discussed in detail in Ref. 32.

## A. Helium

He discharges have been simulated both with and without helium metastable atoms  $\text{He}^*$ . A comparison of these results gives an indication of the relative importance of Penning ionization ( $\text{He}^* + \text{He}^* \rightarrow \text{He}^+ + \text{He} + e$ ) and multistep ionization ( $e + \text{He}^* \rightarrow \text{He}^+ + e + e$ ) compared to primary electron-impact ionization ( $e + \text{He} \rightarrow e + e + \text{He}^+$ ). The electron-impact cross sections for excitation and ionization of  $\text{He}^*$  are many tens of  $\text{\AA}^2$ , and represent an inelastic energy loss having a threshold  $< 5$  eV. The EED can therefore be directly affected by the presence of  $\text{He}^*$ . Collisions of electrons with excited states are included in the EMCS using the modified null cross-section technique.

Representative results for He are shown in Figs. 3–6. Where possible, we have compared our He results with experimental measurements made in the GEC reference cell.<sup>34–36</sup> Our choice of electrode gap,  $2.54 \text{ cm} = 1 \text{ in.}$ , was made on this basis. The results for He shown in these have the same general features as obtained in previous published models of rf noble gas discharges; we present them here to illustrate the basic features of rf discharges.

The instantaneous electric field and electron density during one half of the rf cycle are shown in Fig. 3 for a gas pressure of 0.5 Torr and applied voltage of 150 V. The discharge parameters are symmetric about the discharge midplane because we assumed that the geometry consists of infinite plane parallel electrodes. At times in the rf cycle that are separated by half of the rf period  $T$ , the left electrode and the right electrode become “cathodic” while the opposite electrode is “anodic.” At times an electrode is “cathodic,” the plasma near the electrode resembles the cathode fall of a dc discharge in that there is a large voltage drop between the electrode and the bulk plasma in the center of the discharge. In Figs. 3(a) and 3(b), the left-hand electrode is cathodic at  $t \approx 0.025T$  while the right electrode is cathodic at  $\approx 0.425T$ . At these times, the electron density is very low and the electric field is strong, exceeding  $700 \text{ V/cm}$ . The apparent sheath thickness is  $0.35 \text{ cm}$ . The central “bulk” plasma is characterized by a high density of electrons and  $\text{He}^+$  ions ( $2\text{--}3 \times 10^{10} \text{ cm}^{-3}$ ) and a weak electric field (few  $\text{V/cm}$ ), both of which are relatively insensitive to the time-varying rf electric field. Electrons diffuse toward the anodic electrode (right electrode at  $\approx 0.025T$ ) where the field is weak, and then are expelled later in the rf cycle when the electrode has become cathodic (right electrode at  $\approx 0.425T$ ). This action efficiently heats the electrons, is sometimes described as “waveriding,”<sup>21</sup> and is a general feature of rf discharges where the rf frequency is a few tens of MHz and the pressure is a few mTorr to a few Torr.

The He metastable density, shown in Fig. 3(c), was calculated in the NCTM portion of the model using electron-impact source rates from the EMCS and the heavy particle reaction rates listed in Table II. The effects of radiation trapping and cascade of excited radiative states to metastable states have been included in an approximate fashion. Two electron-impact excitation collisions are included in the present model, a composite collision cross

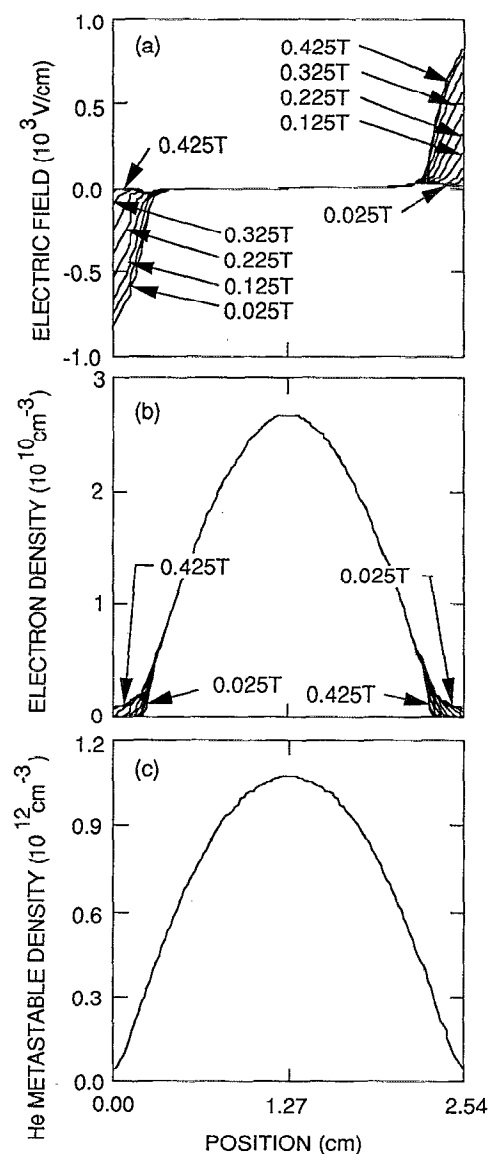


FIG. 3. Computed parameters for a 0.5 Torr He discharge with 150 V applied rf potential (amplitude). The (a) electric field and (b) electron density are shown as a function of position for ten instants during the first half of the rf cycle. The other half of the rf cycle can be constructed by symmetry. The length of the rf period is denoted by  $T$ . (c) The density of the composite He metastable level  $\text{He}^*$ . Volumetric losses for  $\text{He}^*$  are not important for these conditions, and so the density profile is diffusion dominated. The jaggedness in this plot is an artifact of the plotting procedure.

section to a metastable level  $\text{He}^*$ , and a second composite cross section to a radiative level  $\text{He}^{**}$  (Table II). The  $\text{He}^*$  and He densities in this discharge are such that Penning ionizations ( $\text{He}^* + \text{He}^* \rightarrow e + \text{He}^+ + \text{He}$ ) and metastable relaxation ( $\text{He}^* + \text{He} \rightarrow \text{He} + \text{He}$ ) are minor loss processes for  $\text{He}^*$  compared to diffusion to the electrodes. The  $\text{He}^*$  spatial profile is therefore diffusion dominated with a maximum value in the center of the discharge of approximately  $10^{12} \text{ cm}^{-3}$ . The maximum  $\text{He}^*$  density was found to be similar in both 0.5 and 1.0 Torr He discharges. In the absence of significant losses of  $\text{He}^*$  by neutral quenching or nonlinear effects such as Penning ionization, the density of

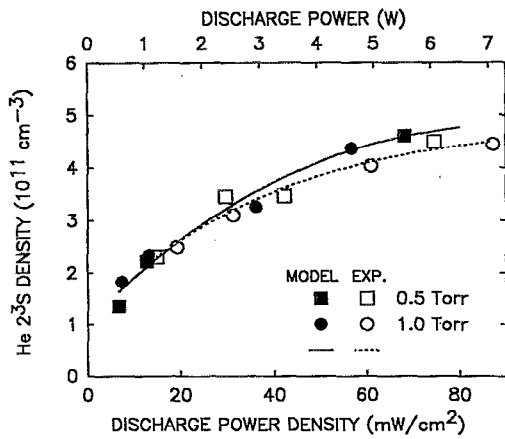


FIG. 4. Computed and experimental values for the average density of the composite He metastable level He\* (model) and He(2<sup>3</sup>S) (experiment) as a function of discharge power density for He gas pressures of 0.5 and 1.0 Torr. For these conditions, the He\* density depends only on power deposition since volumetric quenching processes are not dominant. The experimental results are from Ref. 36. Our computed values have been multiplied by 0.66.

He\* depends only upon discharge power, as shown in Fig. 4. Here we have plotted the density of our composite state and experimental<sup>36</sup> results for the density of He(2<sup>3</sup>S) as a function of power. Our computed results have been multiplied by 0.66 to account for differences between our composite state and He(2<sup>3</sup>S).

The current-voltage waveforms for the discharge conditions of Fig. 3 are shown in Fig. 5. The *V-I* characteristic for discharges in this operating regime are dominated by the capacitance in the sheath regions. The resistive (collisional) bulk plasma is a small component of the overall impedance. The current waveforms for the He discharges presented here typically lead the voltage by 80°–85° and are dominantly sinusoidal. The amplitude of the third harmonic (frequency of 3*f*<sub>0</sub>, where *f*<sub>0</sub> is the fundamental 13.56 MHz) is 5%–10% of the fundamental. The even harmonics (2*n**f*<sub>0</sub>, where *n* is an integer) have zero ampli-

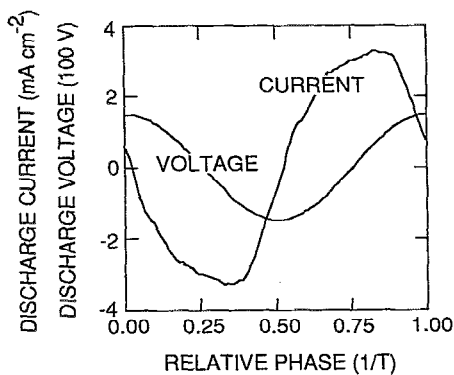


FIG. 5. The voltage-current waveform for the 0.5 Torr He rf discharge with a 150 V (amplitude) applied potential. The discharge is dominantly capacitive, with a phase difference of 80°–85° between voltage and current.

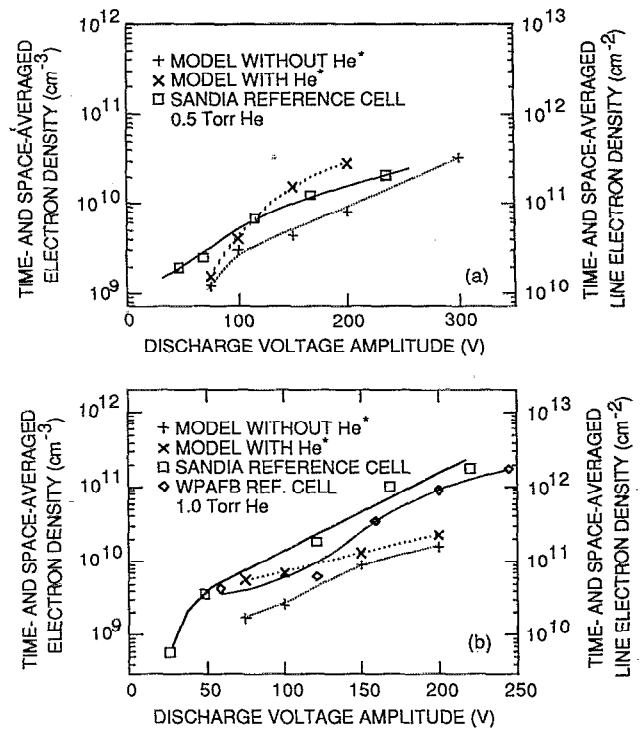


FIG. 6. The time- and space-averaged electron density for (a) 0.5 and (b) 1.0 Torr rf discharges in He. The electrode gap is 2.54 cm. Computed results are shown for cases where helium metastables are included and excluded in the calculation. Microwave interferometry measurements of the line electron density from two GEC reference cells are plotted for comparison.

tude because the model discharge is symmetric about the midplane.

The computed electron densities for 0.5 and 1.0 Torr He discharges are shown in Fig. 6 as a function of rf voltage. Results are shown for two cases, both including and not including metastable He atoms in the calculation. The calculated contributions of Penning reactions and multistep ionization increases the electron density by a factor of 2–3 over the range of conditions studied. The dominant additional contributions to ionization are Penning reactions, with multistep ionization contributing about 5% that of the Penning process. At 0.5 Torr, the incremental contributions of He\* to ionization increase with increasing discharge voltage, whereas at 1.0 Torr the incremental contributions appear to decrease. We attribute this trend to the excitation of the He\* being more localized at the sheath edge at the higher pressure, whereas the losses of He\*, particularly by superelastic electron collisions, are maximum in the bulk plasma.

Experimental measurements of line electron density from two GEC reference cells<sup>34</sup> are also plotted in Fig. 6.<sup>35,36</sup> In order to compare a time- and space-averaged electron density from the model (in units of cm<sup>-3</sup>) and the line-of-sight density from the microwave interferometry measurements (in units of cm<sup>-2</sup>) we must assume a profile for the plasma as a function of radius. We assumed that the plasma has no radial variation within in the 2.54 cm gap between the 10.16-cm-diam GEC reference cell elec-

trodes, and that there is no plasma outside the 10.16-cm-diam cylinder defined by the electrodes. We note, however, that any comparisons are made with the knowledge that the infinite-parallel-plate geometry assumed in the model is only an approximation to the actual GEC reference cell. The reference cell is not a symmetric system, as indicated by the presence of a substantial second harmonic content in the measured reference cell current waveform.<sup>66</sup>

Our calculated results are in fairly good agreement with the measured electron density values for discharge voltages up to  $\approx 300$  V at 0.5 Torr and 175 V at 1.0 Torr. Above these voltages (which correspond to a discharge power density of  $\approx 100$  mW cm<sup>-2</sup>) it is likely that secondary electron emission from the electrodes due to ion, photon, and metastable bombardment becomes significant, and that the discharge becomes more  $\gamma$  like<sup>9</sup> (that is, the ionization that sustains the discharge is driven by energetic electrons that are released from the cathodic electrode and accelerated in the strong sheath fields). The secondary coefficient is not well known for anything but pristine noble gas dischargers and clean electrodes,<sup>67</sup> and we have not included the effects of secondary emission in any of the results present here.

## B. Nitrogen

N<sub>2</sub> plasmas have been modeled to illustrate the characteristics of discharges in electropositive molecular gases. Like He, N<sub>2</sub> does not form a significant density of negative ions. The discharge is therefore electropositive, and the bulk plasma is characterized by approximately equal densities of electrons and positive ions. Unlike He, however, dissociative recombination is a significant loss channel for the positive ions in N<sub>2</sub> discharges. Specifically, N<sub>2</sub><sup>+</sup> can dissociatively recombine to form two neutral N atoms, and it can also associate with N<sub>2</sub> to form N<sub>4</sub><sup>+</sup>, which itself can dissociatively recombine (see Table II). He<sup>+</sup> recombination proceeds only through the three-body neutral or electron-stabilized recombination mechanisms. For these pressures, recombination in He discharges is a minor loss process in comparison to diffusion to the electrodes. Significant volume loss processes for ions in N<sub>2</sub> allow local minima to occur in the charge density profiles and for positive ion-trapping field reversals to form. These structures are simply not allowed in a periodic steady-state He discharge.

Typical results for a N<sub>2</sub> discharge are shown in Fig. 7 for a gas pressure of 1 Torr and a discharge voltage of 150 V. The time-averaged charge density is  $4\text{--}5 \times 10^9$  cm<sup>-3</sup> and average electron temperature is approximately 0.54 eV. Time-averaged electrostatic traps for positive ions exist near the boundary between the sheath and the bulk plasma. The net flow of N<sub>2</sub><sup>+</sup> and N<sub>4</sub><sup>+</sup> ions into these traps is offset (over an rf cycle) by the dissociative recombination processes described above. The cross sections for these processes scale at approximately  $\epsilon^{-1}$ ,<sup>52</sup> and at the low electron temperatures of these discharges, the rate coefficients for dissociative recombination of N<sub>2</sub><sup>+</sup> and N<sub>4</sub><sup>+</sup> are  $4 \times 10^{-8}$  and  $3 \times 10^{-7}$  cm<sup>3</sup> s<sup>-1</sup>, respectively. N<sub>4</sub><sup>+</sup> is formed in an N<sub>2</sub> stabilized three-body reaction. It is there-

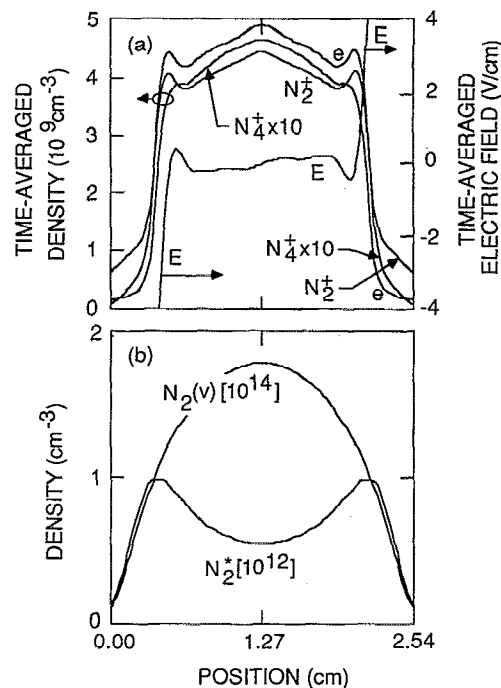


FIG. 7. Results from the hybrid model for a 1.0 Torr N<sub>2</sub> rf discharge (2.54 cm gap) with a 150 V applied discharge potential (amplitude). (a) Charged particle densities and electric field, (b) densities of the composite metastable (N<sub>2</sub><sup>\*</sup>) and composite vibrational [N<sub>2</sub>(*v*)] levels. See Ref. 68 for the plotting methodology. Volumetric loss processes for positive ions (dissociative recombination) enable there to be time-averaged field reversals. Volumetric losses (superelastic relaxation, multistep ionization, and heavy particle quenching) deplete the density of N<sub>2</sub><sup>\*</sup> in the bulk plasma.

fore surprising that for a pressure as low as 1 Torr the N<sub>4</sub><sup>+</sup> has a density approximately 10% of the dimer ion, even though it is formed in a three-body collision and has a higher rate of recombination.

Two minor neutral species are considered in this calculation, a composite electronic metastable level N<sub>2</sub><sup>\*</sup> and a composite vibrationally excited level N<sub>2</sub>(*v*) (see the note in Table II). The density profile of the vibrationally excited species [Fig. 7(b)] indicates that these internally excited neutral species are lost primarily by diffusion to the electrodes. The *V-T* (vibrational-to-translational) relaxation and electron superelastic rates are low. Volumetric losses of N<sub>2</sub>(*v*) are therefore minor in comparison to diffusion. The excitation of N<sub>2</sub><sup>\*</sup> is maximum near the sheath edge and nearly zero at the midplane. There are, however, significant volumetric loss processes for N<sub>2</sub><sup>\*</sup>. These are collisional quenching with N<sub>2</sub>, energy pooling with other N<sub>2</sub><sup>\*</sup>, and superelastic electron collisions with the relatively high density of cool bulk electrons. The net result is that there is a minimum in the density of N<sub>2</sub><sup>\*</sup> at the midplane.

Time- and space-averaged densities for electrons, N<sub>2</sub>(*v*), N<sub>2</sub><sup>\*</sup>, N<sub>2</sub><sup>+</sup>, and N<sub>4</sub><sup>+</sup>, are shown in Fig. 8 for a 1.0 Torr N<sub>2</sub> plasma as a function of discharge power density. All densities increase with increasing power density except that for N<sub>4</sub><sup>+</sup>. The fractional N<sub>4</sub><sup>+</sup> density decreases with increasing power and electron density, apparently due to its higher rate of recombination. All densities scale

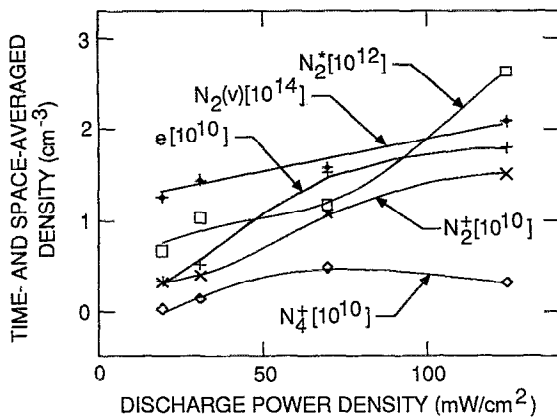


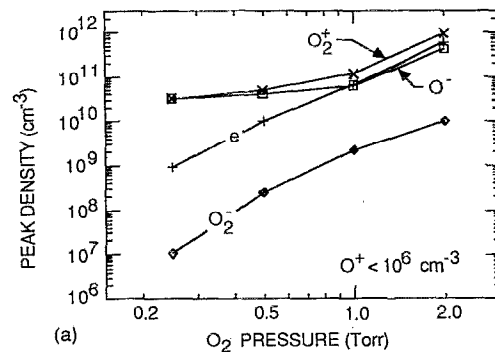
FIG. 8. The time- and space-averaged electron density for various rf discharge voltage amplitudes in  $N_2$ . The pressure is 1.0 Torr and the electrode gap is 2.54 cm. See Ref. 68 for the plotting methodology.

smoothly with power except that for  $N_2^+$ , which increases sharply at higher discharge power. This is a reflection of a rapid increase in the  $N_2^+$  density near the sheath edge, which results from a higher electron temperature there. Due to the resonant character of the excitation cross section for  $N_2(A)$ , its excitation rate appears to be more sensitive to moderate changes in the EED.

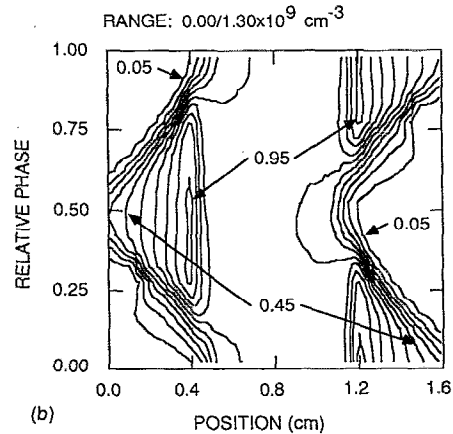
### C. Oxygen

Discharges for various pressures in  $O_2$  have been modeled to illustrate hybrid model predictions for a homogeneous electronegative gas. The electrode spacing for the  $O_2$  cases is 1.6 cm. The predicted peak densities of charged species are plotted in Fig. 9 as a function of  $O_2$  pressure. The time-averaged electron densities and electron temperatures are shown in Fig. 10. At 2 Torr, the  $O_2$  discharge behaves much like the electropositive He and  $N_2$  discharges described above. The densities of electrons and positive ions ( $O_2^+$ ) are nearly equal and the electron temperature is low (0.2 eV) in the bulk plasma. The electron temperature increases with decreasing pressure, both near the sheath edges and at lower pressures; however, the discharge becomes very electronegative. The bulk plasma is still quasineutral, but a negative ion species ( $O^-$ ) balances the positive ion species ( $O_2^+$ ). The electron charge density is low in comparison, but must still carry the discharge current in the bulk plasma. The electrons therefore rush back and forth through the bulk plasma during the rf cycle, as shown in Fig. 9(b), and have a high temperature relative to the more electropositive high-pressure case [Fig. 10(b)].

Negative ions are confined to the bulk plasma by the rf sheaths and are lost primarily in ion-ion neutralization collisions in the plasma volume. As in the  $N_2$  discharges, the existence of significant volume loss processes (ion-ion neutralization and dissociative recombination) allows for time-averaged electrostatic traps for positive ions and local spatial minima in the charged particle densities. This is shown in Fig. 10(a) where the electron density (nearly



(a)



(b)

FIG. 9. Charged particle densities in  $O_2$  rf discharges. (a) Peak charged particle density for various pressures in  $O_2$ . (b) Electron density as a function of position and phase for 0.25 Torr. The electrode gap is 1.6 cm and the discharge rf voltage amplitude is 200 V. The discharge is electronegative at low pressures, but resembles an electropositive discharge at high pressure. The  $O^+$  density is always small in comparison. See Ref. 68 for plotting methodology.

equal to the positive ion density) has a maximum at the sheath edge which is maintained through nearly the entire rf cycles for pressures  $>0.5$  Torr. There is, then, a net diffusion of electrons and positive ions toward the midplane that is balanced over an rf cycle by volumetric losses (recombination and attachment).

Electric fields as a function of location and phase for the four  $O_2$  discharges are presented in Fig. 11. (See Ref. 68 for an explanation of the plotting methodology.) For relatively low  $O_2$  pressures (0.25 Torr) the sheath fields penetrate a maximum of  $\approx 0.48$  cm into the discharge volume, and double layers are maintained at this location for most of the rf cycle. As the  $O_2$  pressure is increased from 0.25 to 2 Torr, the maximum extent of the rf sheaths into the discharge volume decreases to  $\approx 0.11$  cm. At higher pressures (1.0 and 2.0 Torr), the electric field in the bulk plasma does not change sign during the rf cycle, and there is a time-averaged electrostatic trap for positively charged species near the discharge midplane. The flow of ions into this trap is balanced over each rf cycle by volume losses, both dissociative recombination as in the  $N_2$  discharges, and by positive ion-negative ion recombination.

The time-averaged electron density is typically maxi-

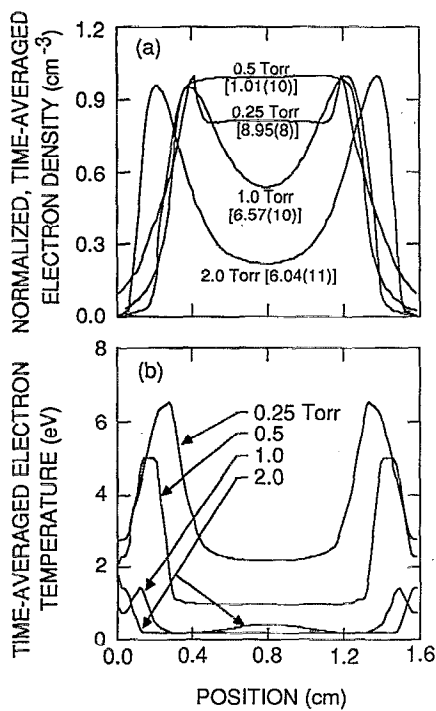


FIG. 10. Time-averaged (a) electron density and (b) electron temperature for various pressures in  $O_2$ . The electron density peaks at the edge of the sheath at higher pressures, a consequence of volumetric losses (attachment and dissociative recombination). The electron temperature increases with decreasing gas pressure, a consequence of the higher effective  $E/N$  and the necessity to offset higher rates of loss by diffusion. See Ref. 68 for the plotting methodology.

imum near the sheath-bulk plasma boundary and reaches a local minimum at the discharge midplane [Fig. 10(a)], particularly at the higher pressures (1.0 and 2.0 Torr). This implies that electron diffusion is acting to push electrons toward the midplane at all times in the rf cycle. The electric field for these conditions does not change sign on either side of the midplane and acts to force electrons toward the electrons. The electric field therefore acts to offset diffusion and to push the electrons away from the midplane toward which they are diffusing. Current continuity is maintained throughout the bulk plasma by a delicate balance of the diffusive and drift components of the electron flux. Small changes in the bulk electric field either allow the net current to flow toward the midplane by diffusion, or toward the electrodes by a combination of drift and diffusion. At 1.0 and 2.0 Torr, the net electron conduction current in the bulk plasma is at many times actually opposed by the bulk electric field. In this respect, the current balance resembles that in a semiconductor  $p$ - $n$  junction.

The electron source rates as a function of  $O_2$  pressure are shown in Fig. 12. These source rates include the contributions of electron impact ionization, attachment, and dissociative recombination. The net local source may then be negative, denoting a sink for electrons at that particular location and phase. At all pressures there exists a net loss of electrons over a majority of the space and time of the rf cycle, a consequence of the lower electron thresholds for attachment and dissociative recombination compared to

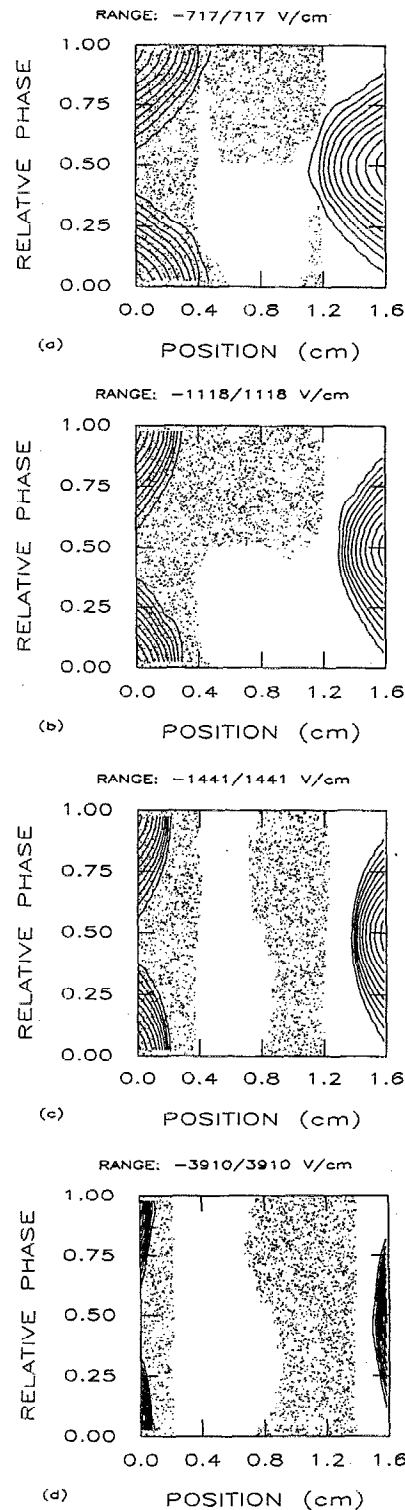


FIG. 11. Electric field contours for various pressures in  $O_2$ . (a) 0.25, (b) 0.5, (c) 1.0, and (d) 2.0 Torr. Contours are equally spaced between the range of values listed at the top of each figure. Clear areas denote positive electric field values; shaded areas denote negative electric field values. The boundary between clear and shaded areas is a field reversal. The labeling scheme for contour plots is explained in Ref. 68.

ionization. The electron source is maximum at the edge of the sheath at the cathodic portion of the rf cycle and extends somewhat across the discharge. The trend is from one of a relatively distributed (in space and time) positive

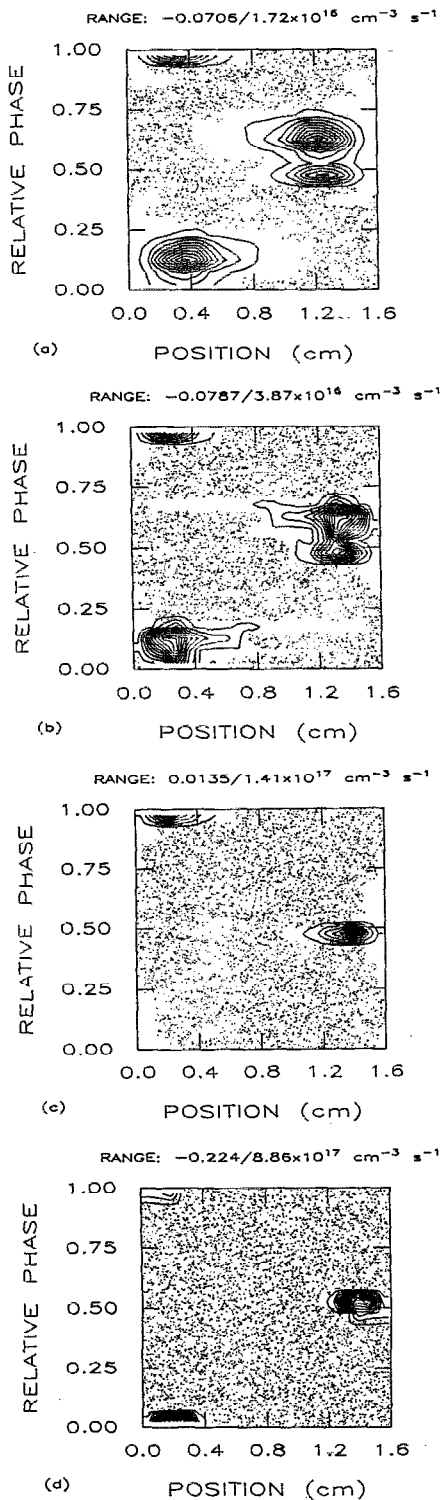


FIG. 12. Total net source rates for electron impact reactions leading to the production or removal of electrons in  $O_2$  for various pressures. (a) 0.25, (b) 0.5, (c) 1.0, and (d) 2.0 Torr. The net rates for electrons are negative during the majority of the rf cycle due to recombination and attachment. The duration and location of the cycle that has positive rates (net ionization) occurs near the edge of the sheath at the cathodic portion of the cycle, and this region constricts as the pressure increases. The labeling scheme for contour plots is explained in Ref. 68.

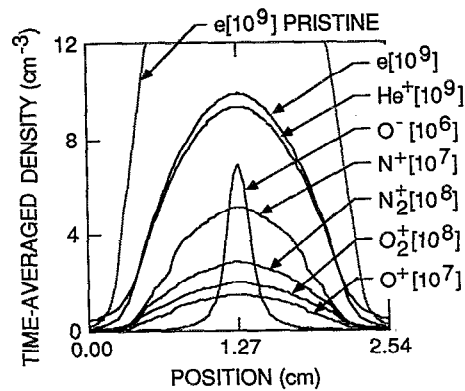


FIG. 13. Time-averaged densities for a He rf discharge contaminated by 100 ppm (parts per million) of dry air. The conditions are otherwise identical to those in Figs. 3–6. The electron density is decreased by a factor of 2 with this small amount of contamination. See Ref. 68 for the plotting methodology.

source at lower pressures to one which is very localized at the maximum extent of the rf sheaths at higher pressures.

#### IV. SIMULATED rf DISCHARGES IN GAS MIXTURES

In this section we present results that demonstrate the ability of the hybrid model to address complex discharge plasmas in gas mixtures. We present results for a dry air-contaminated He discharge ( $He/N_2/O_2$ ), an etching gas mixture ( $He/CF_4/O_2$ ), and  $SiH_4/NH_3$  mixtures appropriate for the deposition of silicon nitride films.

##### A. $He/N_2/O_2$

Contaminants in He discharges have long hampered attempts to measure He swarm parameters because the numerous metastable He atoms have sufficient internal energy to ionize all other gas phase neutrals.<sup>69</sup> He discharges are particularly sensitive to molecular impurities. This sensitivity results from there being no electron inelastic loss processes in He at energies  $< 20$  eV (other than multistep excitation), no appreciable recombination, and no attachment. All processes are possible with a small amount of a molecular impurity.

A  $He/N_2/O_2$  gas mixture has been modeled to illustrate the changes to the pristine He discharges presented in Figs. 3–6 that may be caused when they are contaminated by 100 ppm (parts per million) of dry air ( $N_2/O_2 = 0.8/0.2$ ). The charge densities in the contaminated He discharge are shown in Fig. 13. The contaminated discharge acts very much like an electropositive He discharge in that charge balance in the bulk is provided by nearly equal densities of electrons and  $He^+$  ions. Contaminant ions,  $N_2^+$  and  $O_2^+$ , comprise approximately 5% of the charge density in the bulk plasma, corresponding to a fractional ionization for the contaminants of a few  $10^{-4}$ . Negative ions such as  $O^-$  are quickly lost through ion-ion recombination with  $He^+$ . The negative ions are strongly confined to the discharge midplane by the positive time-averaged plasma potential. The  $N_2^+$  densities here are sufficiently low that three-body collisions leading to  $N_4^+$  are negligible.

The most radical change to the He discharge with air contamination is the absolute plasma density, which has decreased by a factor of  $\approx 2$  compared to the pristine case. This occurs in spite of the addition of species ( $N_2$  and  $O_2$ ) that have a lower ionization threshold energy. The presence of  $N_2$  and  $O_2$  reduces the number of high-energy electrons ("lowers the tail" of the EED) and results in a lower rate of ground state He ionization. He metastable atoms are lost when they ionize the contaminants, but this should not directly affect the  $He^+$  production rate because metastable-metastable ionization ( $He^* + He^* \rightarrow He^+ + He + e$ ) does not greatly contribute to the overall  $He^+$  production for these conditions. The loss rate of  $He^*$  during collisions with the contaminant gases is insufficient to significantly alter the *shape* of the  $He^*$  spatial profile. The *absolute*  $He^*$  density in the contaminated discharge is approximately half that of the pristine case.

### B. He/ $CF_4$ / $O_2$

We present here results for a discharge having equal parts  $CF_4$  and  $O_2$  buffered with He. The He/ $O_2$  chemistry has already been illustrated in the air-contaminated He discharge just presented.  $CF_4$  is an interesting addition to the fill gas mixture because  $CF_4$  does not form a stable ion, either positive or negative.  $CF_4$  can be ionized to form  $CF_3^+$  during collisions with  $He^*$  or  $He^+$ , but not during interactions with  $O_2^+$  or  $O^+$ . However, the  $CF_3^+$  fragment has insufficient internal energy to ionize any other fill gas atom or molecule.

Results for the He/ $CF_4$ / $O_2$  mixture are shown in Fig. 14. The discharge is distinctly electronegative, with the electron density [Fig. 14(a)] an order of magnitude lower than the total positive ion density. The threshold energy for  $He^+$  production is high, and the  $He^+$  density is therefore nearly two orders of magnitude lower than that for  $CF_3^+$ ,  $F^-$ ,  $O_2^+$ ,  $O^+$ , or  $O^-$ , despite the gas mixture, which is 90% He [Fig. 14(b)].  $He^+$  is produced in significant quantities only near the rf sheath. It is quickly lost by charge exchange to both  $O_2$  and  $CF_4$ , and by ion-ion recombination in the bulk plasma.

The  $V$ - $I$  characteristic for this discharge is shown in Fig. 14(c). The discharge is very capacitive, with a nearly sinusoidal current waveform, which leads the voltage by  $75^\circ$  and has  $<5\%$  third harmonic content. This result is perhaps surprising, but it is typical of the gas mixtures and conditions studied. The  $V$ - $I$  characteristic is not very sensitive to drastic changes in the discharge chemistry or operating conditions.

### C. $SiH_4/NH_3$

$SiH_4/NH_3$  gas mixtures are often used for the plasma deposition of  $Si_3N_4$  dielectric films for microelectronics fabrication.<sup>71</sup> The typical discharge conditions are gas pressures of a few hundred mTorr and gas mixtures that are lean in  $SiH_4$ . These discharges are somewhat unique in that the deposition precursor is not a product of direct electron impact of the feedstock gases, but is rather a product of

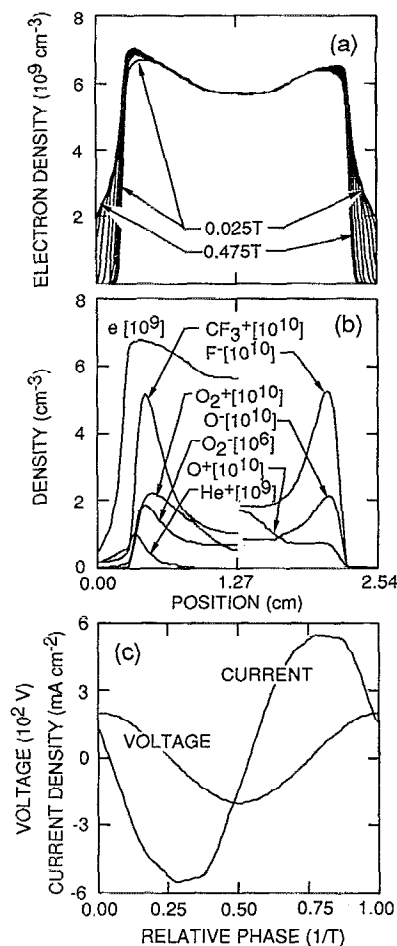
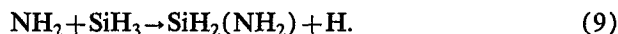
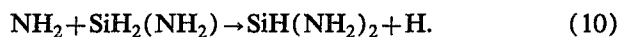


FIG. 14. Results from a 1 Torr He/ $CF_4$ / $O_2 = 0.9/0.05/0.05$  gas mixture, 200 V rf voltage amplitude. (a) The electron density for ten instants during one half of the rf cycle, (b) the time-averaged charged particle densities, and (c) the  $V$ - $I$  characteristic.

reactions between radicals. It is believed that major precursors to  $Si_3N_4$  deposition are amino-silane complexes, initially formed by reaction between  $SiH_3$  and  $NH_2$  radicals,<sup>71,72</sup>



Higher-order precursors are formed by successive insertion reactions by  $NH_2$ , for example,



The  $NH_2$  and  $SiH_3$  radicals are formed by either electron impact dissociation of the feedstock gases ( $NH_3$  and  $SiH_4$ ) or, in the case of  $SiH_3$ , by hydrogen abstraction<sup>32</sup>



The reaction hierarchy in these deposition plasmas can be quite complex.<sup>33</sup>

To examine these deposition plasmas, rf discharges in  $SiH_4/NH_3$  mixtures have been simulated using the hybrid model, and the results have been used as input to a companion plasma chemistry model. Only reactions that affect charged particle production, transport, and loss have been included in the NCTM and SCFM of the hybrid model for

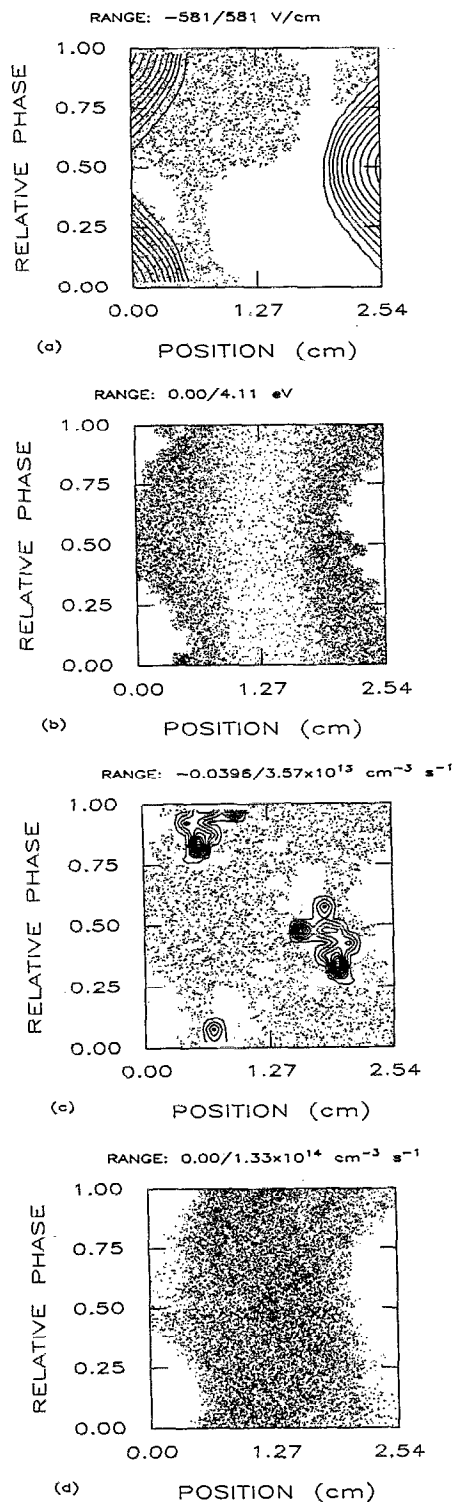


FIG. 15. Plasma parameters for rf discharge in  $\text{SiH}_4/\text{NH}_3 = 0.1/0.9$  at 0.2 Torr. (a) Electric field, (b) electron temperature, (c) net source/sink rate for electron impact reactions leading to the production or removal of  $\text{SiH}_3$ , and (d) rate of dissociative attachment  $e + \text{NH}_3 \rightarrow \text{NH}_2 + \text{H}^-$ . The results are representative for all  $\text{SiH}_4/\text{NH}_3$  mixtures presented here. The labeling scheme for contour plots is explained in Ref. 68.

the reasons discussed in Sec. II D. Representative results from the  $\text{SiH}_4/\text{NH}_3$  discharges are shown in Fig. 15 for a 200 mTorr mixture of  $\text{SiH}_4/\text{NH}_3 = 0.1/0.9$ . The electric field, shown in Fig. 15(a), has a double layer as the rf

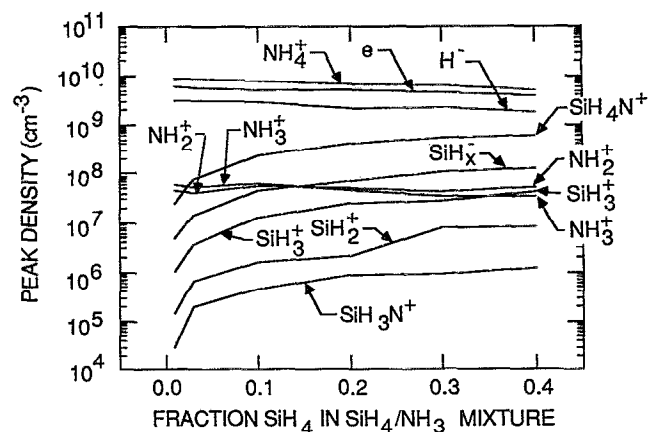
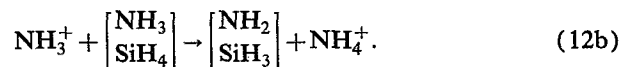
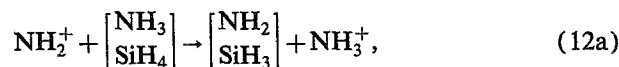


FIG. 16. The peak charged particle densities as a function of  $\text{SiH}_4$  fraction in the  $\text{SiH}_4/\text{NH}_3$  discharges. The electrode gap is 2.54 cm. Due to the lower ionization potential of  $\text{NH}_3$  and the rapid rate of charge exchange leading to formation of  $\text{NH}_4^+$ , even discharges having nearly half  $\text{SiH}_4$  resemble  $\text{NH}_3$  plasmas.

sheath contracts from its maximum extent. The electron temperature, shown in Fig. 15(b), is high ( $\approx 4$  eV) when and where the rf sheaths expand into the discharge volume, but relatively low and constant ( $\approx 0.4$  eV) in the bulk plasma near the discharge midplane. The net electron-impact source rate for  $\text{SiH}_3^+$  is shown in Fig. 15(c) and consists of the sum of its production during electron impact of ground state  $\text{SiH}_4$  ( $e + \text{SiH}_4 \rightarrow e + \text{SiH}_3^+ + \text{H}$ ) and its loss through dissociative recombination ( $e + \text{SiH}_3^+ \rightarrow \text{SiH}_2 + \text{H}$ ). The former process has a high threshold energy (15.4 eV) and therefore occurs only where the electron energy is high, near the expanding sheaths. Dissociative recombination occurs throughout the rf cycle since this process has zero threshold energy. In contrast, the rate for dissociative attachment of electrons to  $\text{NH}_3$  ( $e + \text{NH}_3 \rightarrow \text{NH}_2 + \text{H}^-$ ) is shown in Fig. 15(d). This process has a low (but nonzero) threshold energy and therefore occurs primarily in the bulk plasma where the electron density is high and the electron temperature is low. The rate for this process is relatively insensitive to the rf variations in the sheaths.

The peak charged particle densities for various  $\text{SiH}_4/\text{NH}_3$  gas mixtures are shown in Fig. 16. These discharges are all relatively similar because to first order they can be thought of as  $\text{NH}_3$  discharges in terms of ion composition. The ionization threshold energy for  $\text{NH}_3$  is lower than that for  $\text{SiH}_4$ , so the dominant electron-impact-produced ions in all cases are products of  $\text{NH}_3$  ( $\text{NH}_2^+$  and  $\text{NH}_3^+$ ). Both of these ions can abstract H from either  $\text{SiH}_4$  or  $\text{NH}_3$  to form either  $\text{NH}_3^+$  or  $\text{NH}_4^+$ :<sup>64</sup>



The negative ion formation rate is at no time sufficient to result in a discharge with electronegative characteristics.

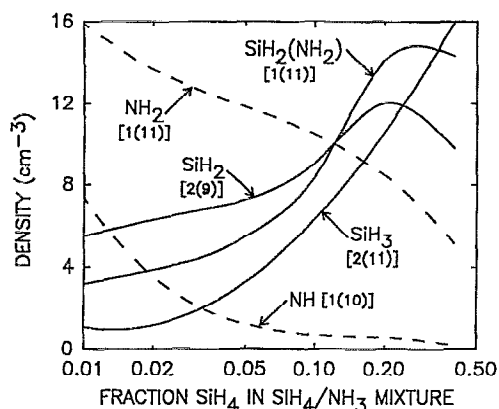


FIG. 17. Volume-averaged densities of minor neutral species as a function of  $\text{SiH}_4$  fraction. A deposition precursor to  $\text{Si}_3\text{N}_4$  is believed to be  $\text{SiH}_2(\text{NH}_2)$ , formed by the reaction between  $\text{SiH}_3$  and  $\text{NH}_2$ . Production of the precursor peaks at a  $\text{SiH}_4$  mole fraction of approximately 0.3. See Ref. 68 for the plotting methodology.

Si-containing ions may react to form  $\text{SiH}_4\text{N}^+$  and  $\text{SiH}_3\text{N}^+$  which cannot charge exchange to form  $\text{NH}_4^+$ , but this reaction pathway is of only minor importance to the overall charge balance. The net result is that most ionizations eventually result in the production of  $\text{NH}_4^+$ , and that the discharge (up to a  $\text{SiH}_4$  mole fraction of 0.5) is always much like a discharge in pure  $\text{NH}_3$ .

The source rates for all electron impact processes from each of these calculations has been used as input to a separate neutral plasma chemistry/flow model in which a comprehensive plasma chemistry reaction scheme has been implemented. Details of the plasma chemical reaction scheme are discussed in Ref. 33. This model presumes that the  $\text{SiH}_4/\text{NH}_3$  gas mixture is admitted to the discharge chamber through a showerhead in one of the electrodes and flows radially outward to a vacuum pump. The species densities are found using the calculated gas flow field, diffusion coefficients, and gas phase reaction rate coefficients.

The results from the hybrid model and the plasma flow/chemistry model are shown in Fig. 17, again as a function of  $\text{SiH}_4/\text{NH}_3$  mixture.  $\text{SiH}_2(\text{NH}_2)$  is thought to be the precursor for high-quality  $\text{Si}_3\text{N}_4$  films, and it forms in association reactions between  $\text{SiH}_3$  (which increases with increasing  $\text{SiH}_4$  fraction) and  $\text{NH}_2$  (which decreases with increasing  $\text{SiH}_4$  fraction).  $\text{NH}$ , which is more reactive with the silane than  $\text{NH}_2$ , decreases in density more quickly with increasing  $\text{SiH}_4$  fraction than  $\text{NH}_2$ . The model predicts a maximum volume-averaged precursor density of  $\approx 1.5 \times 10^{12} \text{ cm}^{-3}$  at a mixture of  $\text{SiH}_4/\text{NH}_3 \approx 0.3/0.7$ .

Details of the gas phase chemistry are shown in Fig. 18. The  $\text{NH}$  density is largest for a pure  $\text{NH}_3$  discharge, but decreases with increasing  $\text{SiH}_4$  fraction because it is lost in reactions with  $\text{SiH}_4$  and  $\text{SiH}_3$  [Fig. 18(a)]. The  $\text{SiH}_2$  density increases with  $\text{SiH}_4$  fraction for low  $\text{SiH}_4$  fraction, but is lost at higher  $\text{SiH}_4$  mole fractions reaction by the insertion reaction  $\text{SiH}_2 + \text{SiH}_4 \rightarrow \text{Si}_2\text{H}_6$  [Fig. 18(b)]. In both of these cases, the radical ( $\text{NH}$  or  $\text{SiH}_2$ ) is lost in reactions with one of the feedstock gases ( $\text{SiH}_4$  or  $\text{NH}_3$ ).

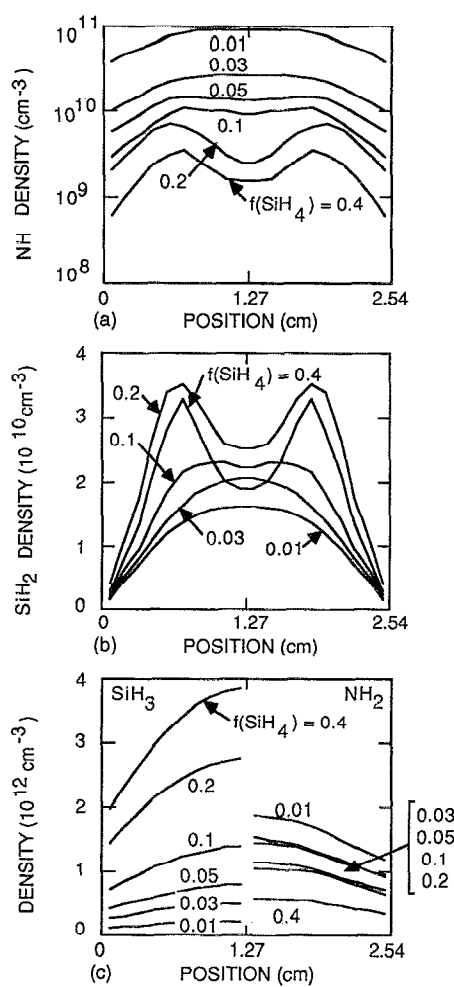


FIG. 18. Minor neutral species density profiles from the companion plasma chemistry/flow model for various  $\text{SiH}_4$  fractions in  $\text{SiH}_4/\text{NH}_3$  mixtures: (a)  $\text{NH}$ , (b)  $\text{SiH}_2$ , and (c)  $\text{SiH}_3$  and  $\text{NH}_2$ .  $\text{NH}$  and  $\text{SiH}_2$  are depleted during gas phase collisions with the fill gases.  $\text{SiH}_3$  and  $\text{NH}_2$  are lost only during collisions with other gas phase radicals and so their densities are diffusion dominated.

Contrast this with the variation in  $\text{SiH}_3$  and  $\text{NH}_2$  density as a function of  $\text{SiH}_4$  fraction, shown in Fig. 18(c). The major gas phase loss mechanisms for these two radicals involve reactions with other gas phase radicals, the density of which is low relative to the feedstock gases. Losses of these radicals are therefore diffusion dominated for all  $\text{SiH}_4$  fractions presented.

## V. SUMMARY AND CONCLUSIONS

In this article we have presented a hybrid model of rf discharges consisting of a Monte Carlo simulation of electron motion, a self-consistent drift-diffusion (fluid) model of charged particle transport, and a neutral chemistry/transport model. We conjectured that such a model should have the quantitative accuracy of a fully self-consistent kinetic simulation (since the electrons are described kinetically) yet execute with the speed of a fluid model. This latter advantage exists because we only require that statistical noise be sufficiently small to obtain the source rates,

and not the much more stringent requirement that the statistical noise be sufficiently small to solve Poisson's equation. We found that computation time is indeed dominated by the self-consistent fluid portion of the model, and that the execution time is therefore comparable to an ordinary drift-diffusion model. The hybrid model predictions are in good quantitative agreement with line electron densities in He discharges measured by microwave interferometry and spectroscopic measurements of excited state densities, verifying that quantitative accuracy is possible by using such a hybrid model. The hybrid model is able to address multiple species systems having complex ion and neutral chemistry.

The neutral transport/chemistry portion of the model allows one to address discharges in gas mixtures where gas phase neutral chemistry is important. Even in discharges in noble gases such as He, which are void of chemistry in the traditional sense, neutral species such as the He metastable can affect the discharge. In the case of He, we observed moderate increases in plasma density and decreases in discharge resistance due to He\* contributions to the total charged particle production through Penning and multi-step ionization. In cases where minor neutral species play no appreciable role in the overall charge balance, accurate modeling of their behavior can still be important because it can provide a convenient point of contact with experiment. For example, absolute He\* densities can be measured with good spatial resolution using a combination of absorption and laser-induced fluorescence spectroscopy.<sup>36</sup> In cases such as the SiH<sub>4</sub>/NH<sub>3</sub> mixtures presented, gas phase radicals are minor species and play minor roles in the charged particle balance, but are of great importance because of their role in the deposition of Si<sub>3</sub>N<sub>4</sub>.

The success of a hybrid model in large part hinges on the degree of "coupling" required between the electron Monte Carlo simulation (EMCS), the self-consistent fluid model (SCFM), and the neutral chemistry/transport model (NCTM). For the results presented here, the SCFM was run for 5–20 rf cycles before returning to the EMCS to obtain updated (quasi-steady-state) electron collision rates. The NCTM (which generates steady-state neutral densities based on the source rates averaged over one rf cycle) is updated at each new SCFM time step. This iterative scheme was successful here in that it is numerically stable and executes in an acceptable amount of computer time. One can imagine instances, however, where this coupling scheme is insufficient to lead to a harmonic steady-state solution. One example is a discharge that is only marginally sustained, such that a small decrease in pressure or rf voltage would result in discharge extinction. In an actual discharge a small decrease in the plasma density leads to greater field penetration into the bulk and a large increase in the ionization rate over a short time (perhaps <1 rf cycle). The source rates in the hybrid model would need to be updated on a similar time scale. In many cases, however, the coupling scheme presented in this article is quite effective.

Results for several homogeneous fill gas discharges were presented. He discharges were presented as a basis of

comparison to previous models and to experimental results from the GEC reference cell. The predicted mean electron density were in good agreement with microwave interferometry measurements for 0.5 and 1.0 Torr He, 2.54 cm gap, and <0.1 W/cm<sup>2</sup> power deposition. He metastable atoms were found to have only a moderate effect on the overall plasma density for these conditions. Several 1.0 Torr N<sub>2</sub> plasmas were presented for the same gap and range of power deposition as He. Dissociative recombination processes absent in He discharges allow for the formation of time-averaged electrostatic traps for the positive ions in N<sub>2</sub>. O<sub>2</sub> discharges for a range of pressures at 200 V peak applied rf voltage were presented as an example of an electronegative discharge. For an electrode gap of 1.6 cm, a 0.25 Torr O<sub>2</sub> discharge was found to be quite electronegative, with the electron density less than 0.03 that of O<sub>2</sub><sup>+</sup> and O<sup>-</sup>, which nearly balance. As the pressure was increased, however, the O<sub>2</sub> discharge became quite electropositive. At 1.0 Torr, the electron density and O<sup>-</sup> density are approximately equal, and above 1.0 Torr, the electron density is greater than the O<sup>-</sup> density. At the same time, the mean electron energy at the discharge midplane fell from >2 eV (0.25 Torr) to ≈0.2 eV (2.0 Torr), as might be expected from the change of the discharge character from electronegative to electropositive.

Discharges in several gas mixtures were presented. A He discharge contaminated with 100 ppm of dry air was found to have a peak plasma density approximately half that of its pristine value. The discharge in other respects was much like a pristine electropositive He discharge in that only minor densities of negative ions were formed. A He/CF<sub>4</sub>/O<sub>2</sub> discharge was presented as an illustration of a typical etching discharge chemistry. Finally, discharges in several SiH<sub>4</sub>/NH<sub>3</sub> mixtures were presented as an illustration of a deposition chemistry. For mixtures up to equal parts SiH<sub>4</sub> and NH<sub>3</sub> (200 mTorr, 200 V, 2.54 cm gap), the SiH<sub>4</sub>/NH<sub>3</sub> discharges were found to be much like discharges in pure NH<sub>3</sub> because most ions in a SiH<sub>4</sub>/NH<sub>3</sub> discharge will charge exchange and abstract H until reaching NH<sub>4</sub><sup>+</sup>. A companion plasma chemistry/flow model of the entire Si<sub>3</sub>N<sub>4</sub> deposition chemistry was used to generate the density of minor radical species that do not affect the discharge dynamics, but that are pivotal to the deposition process.

## ACKNOWLEDGMENTS

The authors would like to acknowledge helpful conversations with M. Barnes, P. Bletzinger, D. B. Graves, K. Greenberg, G. Hebner, W. N. G. Hitchon, P. Hargis, J. Keller, M. A. Lieberman, and J. T. Verdeyen. We would also like to thank K. James who aided in program development. The authors express special thanks to K. Greenberg and G. Hebner of Sandia National Laboratory for sharing their experimental results prior to publication. This work was supported by the IBM East Fishkill Facility, the National Science Foundation, the University of Wisconsin Engineering Research Center for Plasma Aided Manufacturing, and the Semiconductor Research Corpo-

ration. The participation of K. James was sponsored by a grant from the National Science Foundation for Research Experiences for Undergraduates.

- <sup>1</sup> *Plasma Etching. An Introduction*, edited by D. M. Manos and D. L. Flamm (Academic, Boston, 1989).
- <sup>2</sup> L. E. Kline and M. J. Kushner, *Crit. Rev. Solid State Mater. Sci.* **16**, 1 (1989); D. B. Graves, *AIChE J.* **35**, 1 (1989).
- <sup>3</sup> A collection of papers on the modeling of collisional low-temperature plasmas can be found in a Special Issue section of *IEEE Trans. Plasma Sci.* **PS-19** (1991).
- <sup>4</sup> R. A. Gottscho, *Phys. Rev. A* **36**, 2233 (1987); T. Nakano, N. Sadeghi, and R. A. Gottscho, *Appl. Phys. Lett.* **58**, 458 (1991); and references therein.
- <sup>5</sup> P. J. Hargis and K. E. Greenberg, *Appl. Phys. Lett.* **53**, 1809 (1988); *J. Appl. Phys.* **67**, 2767 (1990); and references therein.
- <sup>6</sup> J. L. Jauberteau, G. J. Meeusen, M. Haverlag, G. M. W. Kroesen, and F. J. deHoog, *J. Phys. D* **24**, 261 (1991); and references therein.
- <sup>7</sup> D. B. Graves and K. F. Jensen, *IEEE Trans. Plasma Sci.* **PS-14**, 78 (1986); D. B. Graves, *J. Appl. Phys.* **62**, 88 (1987).
- <sup>8</sup> P. Bayle, J. Vacquie, and M. Bayle, *Phys. Rev. A* **34**, 360 (1986).
- <sup>9</sup> Ph. Belenguer and J. P. Boeuf, *Phys. Rev. A* **41**, 4447 (1990).
- <sup>10</sup> D. B. Graves, T. E. Nitschke, and M. Surendra, Abstract DB-6, 44th Gaseous Electronics Conference, Albuquerque, NM, October 1991.
- <sup>11</sup> R. W. Boswell and I. J. Morey, *Appl. Phys. Lett.* **52**, 21 (1988).
- <sup>12</sup> M. Surendra and D. B. Graves, *IEEE Trans. Plasma Sci.* **PS-19**, 144 (1991).
- <sup>13</sup> T. J. Sommerer, W. N. G. Hitchon, R. E. P. Harvey, and J. E. Lawler, *Phys. Rev. A* **43**, 4452 (1991).
- <sup>14</sup> S. M. Levitskii, *Zh. Tekh. Fiz.* **27**, 970 (1957) [*Sov. Phys. Tech. Phys.* **2**, 887 (1957)].
- <sup>15</sup> V. A. Godyak and A. S. Khanneh, *IEEE Trans. Plasma Sci.* **PS-16**, 112 (1986).
- <sup>16</sup> N. Sato and H. Tagashira, *IEEE Trans. Plasma Sci.* **PS-19**, 102 (1991).
- <sup>17</sup> M. Surendra, D. B. Graves, and G. M. Jellum, *Phys. Rev. A* **41**, 1112 (1990).
- <sup>18</sup> Karl H. Schoenbach, Hao Chen, and G. Schaefer, *J. Appl. Phys.* **67**, 154 (1990).
- <sup>19</sup> R. K. Porteous and D. B. Graves, *IEEE Trans. Plasma Sci.* **PS-19**, 204 (1991).
- <sup>20</sup> Y. Weng and M. J. Kushner, Semiconductor Research Corporation Report C91695, 1991.
- <sup>21</sup> M. J. Kushner, *J. Appl. Phys.* **54**, 4958 (1983); M. J. Kushner, *IEEE Trans. Plasma Sci.* **PS-14**, 188 (1986).
- <sup>22</sup> C. G. Goedde, A. J. Lichtenberg, and M. A. Lieberman, *J. Appl. Phys.* **64**, 4375 (1988).
- <sup>23</sup> M. Surendra and D. B. Graves, *Phys. Rev. Lett.* **66**, 1469 (1991).
- <sup>24</sup> V. A. Godyak and R. B. Piejak, *Phys. Rev. Lett.* **65**, 996 (1990).
- <sup>25</sup> J. P. Boeuf, *Phys. Rev. A* **36**, 2782 (1987).
- <sup>26</sup> R. J. Kee and J. A. Miller, Sandia National Laboratory Report SAND86-8841, 1986.
- <sup>27</sup> H. W. Ellis, R. Y. Pai, E. W. McDaniel, E. A. Mason, and L. A. Viehland, *At. Data Nucl. Data Tables* **17**, 177 (1976); H. W. Ellis, E. W. McDaniel, D. L. Albritton, L. A. Viehland, S. L. Lin, and E. A. Mason, *At. Data Nucl. Data Tables* **22**, 179 (1978); H. W. Ellis, M. G. Thackston, E. W. McDaniel, and E. A. Mason, *At. Data Nucl. Data Tables* **31**, 133 (1984).
- <sup>28</sup> M. S. Barnes, T. J. Colter, and M. E. Elta, *J. Appl. Phys.* **61**, 81 (1987).
- <sup>29</sup> H. R. Skullerud, *J. Phys. D* **1**, 1567 (1968).
- <sup>30</sup> S. L. Lin and J. N. Bardsley, *J. Chem. Phys.* **66**, 435 (1977).
- <sup>31</sup> Y. Weng and M. J. Kushner, *Phys. Rev. A* **42**, 6192 (1990).
- <sup>32</sup> M. J. Kushner, *J. Appl. Phys.* **63**, 2532 (1988).
- <sup>33</sup> M. J. Kushner, Semiconductor Research Corporation Report C91698, 1991.
- <sup>34</sup> Anonymous, *Bull. Am. Phys. Soc.* **34**, 295 (1989); P. J. Hargis, Jr., K. E. Greenberg, P. A. Miller, J. B. Gerardo, R. A. Gottscho, A. Garscadden, P. Bletzinger, J. R. Roberts, J. K. Olthoff, J. R. Whetstone, R. J. Van Brunt, H. M. Anderson, M. Splichal, J. L. Mock, M. L. Passow, M. L. Brake, M. E. Elta, D. B. Graves, M. J. Kushner, J. T. Verdeyen, G. Selwin, M. Dalvie, J. W. Butterbaugh, H. H. Sawin, T. R. Turner, and R. Horwath, *Bull. Am. Phys. Soc.* **36**, 195 (1991).
- <sup>35</sup> P. Bletzinger and A. Garscadden, *IEEE Conference on Plasma Science, Williamsburg, VA*, 3-5 June 1991.
- <sup>36</sup> G. A. Hebner and K. E. Greenberg, Abstract AA-1, 44th Gaseous Electronics Conference, Albuquerque, NM, 22-25 October 1991.
- <sup>37</sup> M. Hayashi, Nagoya Institute of Technology Report IPPJ-AM-19, Gokiso-cho, Showa-ku, Nagoya 466, Japan.
- <sup>38</sup> J. P. Boeuf and E. Marode, *J. Phys. D* **15**, 2169 (1982).
- <sup>39</sup> D. Rapp and P. Englander-Golden, *J. Chem. Phys.* **43**, 1464 (1965).
- <sup>40</sup> W. C. Fon, K. A. Berrington, P. G. Burke, and A. E. Kingston, *J. Phys. B* **14**, 2921 (1981).
- <sup>41</sup> L. Vriens, *Phys. Lett.* **8**, 260 (1964).
- <sup>42</sup> M. Mitchner and C. H. Kruger, Jr., *Partially-Ionized Gases* (Wiley, New York, 1973).
- <sup>43</sup> M. A. Biondi, in *Principles of Laser Plasmas*, edited by G. Bekefi (Wiley, New York, 1976), pp. 125-158.
- <sup>44</sup> R. Deloche, P. Monchicourt, M. Cheret, and F. Lambert, *Phys. Rev. A* **13**, 1140 (1976).
- <sup>45</sup> A. V. Phelps, *Phys. Rev.* **99**, 1307 (1955).
- <sup>46</sup> L. S. Frost and A. V. Phelps, *Phys. Rev.* **127**, 1621 (1967).
- <sup>47</sup> G. J. Schulz, *Phys. Rev.* **135**, A988 (1964); D. Spence, J. L. Mauer, and G. J. Schulz, *J. Chem. Phys.* **57**, 5516 (1972).
- <sup>48</sup> W. L. Borst, *Phys. Rev. A* **5**, 648 (1972).
- <sup>49</sup> D. C. Cartwright, S. Trajmar, A. Chutjian, and W. Williams, *Phys. Rev. A* **16**, 1041 (1977).
- <sup>50</sup> R. T. Brinkmann and S. Trajmar, *Ann. Geophys.* **26**, 201 (1970).
- <sup>51</sup> A. V. Phelps and L. C. Pitchford, *Phys. Rev.* **31**, 2932 (1985); and references therein.
- <sup>52</sup> J. B. A. Mitchell, *Phys. Rep.* **186**, 215 (1990).
- <sup>53</sup> L. G. Piper, *J. Chem. Phys.* **88**, 231 (1988).
- <sup>54</sup> L. G. Piper, *J. Chem. Phys.* **87**, 1625 (1987).
- <sup>55</sup> D. L. Albritton, *At. Nucl. Data Tables* **22**, 1 (1978).
- <sup>56</sup> A. V. Phelps, JILA Information Center Report No. 28, University of Colorado, Boulder, CO (1985).
- <sup>57</sup> J. T. Moseley, R. E. Olson, and J. R. Peterson, *Case Studies At. Phys.* **5**, 1 (1975).
- <sup>58</sup> E. W. McDaniel, V. Čermák, A. Dalgarno, E. E. Ferguson, and L. Friedman, *Ion Molecule Reactions* (Wiley, New York, 1970).
- <sup>59</sup> Y. Itikawa, A. Ichimura, K. Onda, K. Sakimoto, and K. Takayanagi, *J. Phys. Chem. Ref. Data* **18**, 23 (1989).
- <sup>60</sup> J. M. Pouvesle, A. Khacef, J. Stevefelt, H. Jahani, V. T. Gylys, and C. B. Collins, *J. Chem. Phys.* **88**, 3061 (1988).
- <sup>61</sup> M. Hayashi, in *Swarm Studies and Inelastic Electron-Molecule Collisions*, edited by L. C. Pitchford, B. V. McKoy, A. Chutjian, and S. Trajmar (Springer, New York, 1987), pp. 167-187.
- <sup>62</sup> E. R. Fisher, M. E. Weber, and P. B. Armentrout, *J. Chem. Phys.* **92**, 2296 (1990).
- <sup>63</sup> J. M. S. Henis, J. Stewart, M. K. Tripodi, and P. P. Gaspar, *J. Chem. Phys.* **57**, 389 (1972).
- <sup>64</sup> M. Hayashi, in *Nonequilibrium Processes in Partially Ionized Gases*, edited by M. Capitelli and M. N. Bardsley (Plenum, New York, 1990), pp. 333-340.
- <sup>65</sup> I. Haller, *J. Phys. Chem.* **94**, 4135 (1990).
- <sup>66</sup> J. R. Roberts, J. K. Olthoff, R. J. Van Brunt, and J. R. Whetstone, *Bull. Am. Phys. Soc.* **36**, 195 (1991).
- <sup>67</sup> E. A. Den Hartog, D. A. Dougherty, and J. E. Lawler, *Phys. Rev. A* **38**, 2471 (1988).
- <sup>68</sup> Numbers in square brackets denote the multiplicative factor that must be applied when reading absolute densities. Contours in the plots are evenly spaced between the minimum and maximum values listed above the figure. The regions shaded by dots indicate that the plotted quantity is negative. Shading on these contour plots merely indicates the sign of the plotted quantity; the magnitude is obtained from the contours. In cases where the plotted quantity is uniformly positive, we may use a "dot plot" to display the data. In this case, the variation of the plotted quantity is shown as a variation in the dot density. White (no dots) corresponding to the lower value listed at the top of the figure, and the darkest (most dots) corresponding to the higher of the listed values.
- <sup>69</sup> J. Dutton, *J. Phys. Chem. Ref. Data* **4**, 577 (1975).
- <sup>70</sup> S. G. Lias, J. E. Bartmess, J. F. Liebman, J. L. Holmes, R. D. Levin, and W. G. Mallard, *J. Phys. Chem. Ref. Data* **17**, Suppl. 1, 1 (1988).
- <sup>71</sup> D. L. Smith, A. S. Alimonda, C.-C. Chen, S. E. Ready, and B. Wacker, *J. Electrochem. Soc.* **137**, 614 (1990).
- <sup>72</sup> D. B. Beach and J. Jansinski, *J. Chem Phys.* **94**, 3019 (1990).